THESIS FOR THE DEGREE OF DOCTOR OF PHILOSOPHY

Sustainable Energy Conversion from Biomass Waste Combustion

Experimental and Multiscale Modelling Studies

Maulana Gilar Nugraha

Department of Chemistry and Chemical Engineering

CHALMERS UNIVERSITY OF TECHNOLOGY

Gothenburg, Sweden 2022

Sustainable Energy Conversion from Biomass Waste Combustion
Experimental and Multiscale Modelling Studies

Maulana Gilar Nugraha
ISBN 978-91-7905-723-7

Doktorsavhandlingar vid Chalmers tekniska högskola
Ny serie nr 5189
ISSN 0346-718X

Department of Chemistry and Chemical Engineering
Chalmers University of Technology
SE-412 96 Gothenburg
Sweden
Telephone + 46 (0)31-772 1000

Cover:
Experimental facility utilized in the current work superposed with contour plot of temperature from CFD simulation. The three encircled figures highlight the reaction bands during biomass devolatilization, film layer due to Stefan flow and soot concentration in the lower part of the furnace.

Printed by Chalmers Digitaltryck
Gothenburg, Sweden 2022

Sustainable Energy Conversion from Biomass Waste Combustion

Experimental and Multiscale Modelling Studies

Maulana Gilar Nugraha
Department of Chemistry and Chemical Engineering
Chalmers University of Technology

ABSTRACT

The development of sustainable energy conversion via residual biomass combustion is one of the scientific and industrial community focus today to fulfilling the global net zero emission commitment in 2050. Despite its potency due to the abundant stock of biomass, hazardous particulate matter (PM) emission from residual biomass combustion remains a big challenge to increase the contribution of biomass combustion as a main renewable energy source. Therefore, this study analyses how particulate matter can be formed and minimized in the system of residual biomass combustion. The study includes multiscale modelling and simulation analysis validated thoroughly using detail and accurate observation in an experimental facility.

To facilitate accurate prediction of particle pyrolysis and combustion, a computationally efficient sub-grid model of biomass particle model is developed. The developed particle model that relies on the orthogonal collocation method and a comprehensive physicochemical mechanism is proven to be accurate based on a high degree of agreement with experimental results for particle pyrolysis and combustion experiments. Improved prediction of mass transfer to and from spherical particles during pyrolysis and combustion is also analyzed in the current work by the correction of Sherwood number due to Stefan flow. High resolved computational fluid dynamics (CFD) analysis confirms that the proposed corrected Sherwood number produced better agreement in comparison to the established Spalding and Abrahamson model.

Grate-fired biomass furnace is designed and constructed in the current work to allow accurate observation of combustion parameters in different combustion conditions. Online spatially resolved PM measurement system allows accurate in-situ measurement of PM reactivity. The steady CFD model validated thoroughly with experimental observation is proven to predict the global behavior of biomass combustion accurately. In addition, a predictive kinetic model for PM reduction was developed using the Discrete Particle Model (DPM) in CFD analysis.

The time-resolved CFD model is also formulated in this study, together with more detailed devolatilization kinetics by the inclusion of different lignocellulosic components. The CFD analysis reveals that 99.3% of the soot is burnt in the combustion chamber. Local concentrations of soot precursors from lignin decomposition i.e., acetylene, and regions with a high temperature in the freeboard promote an increased rate of soot formation. Meanwhile, the residence time and oxygen availability become the most influential factors to minimize the soot emissions.

Keywords: *biomass, combustion, particulate matter, soot, CFD simulation, furnace, orthogonal collocation, Stefan flow*.

List of Publications:

This thesis is based on the content of the following appended papers:

I. Nugraha, M.G., Saptoadi, H., Hidayat, M., Andersson, B., Andersson, R. Particle modelling in biomass combustion using orthogonal collocation. Applied Energy 2019, 255, 113868. https://doi.org/10.1016/j.apenergy.2019.113868.

II. Nugraha, M.G., Andersson, R., Andersson, B. On the Sherwood number correction due to Stefan flow. Chemical Engineering Science 2022, 249, 117292. https://doi.org/10.1016/j.ces.2021.117292.

III. Nugraha, M.G., Saptoadi, H., Hidayat, M., Andersson, B., Andersson, R. Particulate Matter Reduction in Residual Biomass Combustion. Energies 2021, 14, 3341. https://doi.org/10.3390/en14113341.

IV. Nugraha, M.G., Saptoadi, H., Hidayat, M., Andersson, B., Andersson, R. Analysis of Particulate Matter Emission in Biomass Combustion, Manuscript.

Contribution Report:

Paper I: First author. I planned and conducted the modelling and simulation works. I analyzed the simulation results together with co-authors. I wrote manuscript together with co-authors.

Paper II: First author. I planned the modelling and simulation works together with the co-authors. I analyzed the simulation results together with co-authors. I wrote the manuscript together with co-authors.

Paper III: First author. I planned and conducted the experimental and simulation works. I analyzed the experiment and simulation results together with co-authors. I wrote the manuscript together with co-authors.

Paper IV: First author. I planned and conducted the experimental and simulation works. I analyzed the experiment and simulation results together with co-authors. I wrote the manuscript together with co-authors.

Acknowledgments

The research presented in this thesis was conducted within the Chemical Engineering Division at Chalmers University of Technology, Sweden and Chemical Engineering and Mechanical Engineering Departments at Universitas Gadjah Mada (UGM), Indonesia. The financial support from the Swedish Research Council is gratefully acknowledged.

I would like to immensely thank many people who have supported me, in particular:

My supervisor, **Prof. Ronnie Andersson**, who gave me the opportunity to be a PhD student within your research group. I am very thankful to have all the encouraging and intensive discussions with you. Your valuable advices really motivated me a lot to be a better researcher.

My co-supervisor, **Prof. Bengt Andersson**, for a lot of wonderful and valuable ideas during research discussions. You are really helping me to see broader perspective of things.

My co-supervisors in Indonesia, **Prof. Harwin Saptoadi** and **Assoc. Prof. Muslikhin Hidayat**, for massive supports to manage experimental works in UGM's lab.

All my colleagues in KRT for creating such a wonderful and enjoyable office.

All my colleagues and seniors in Departemen Teknik Kimia UGM, for all the support during my study period.

All my former bachelor students in UGM who have helped me to run the experiments in Indonesia.

All current and former Indonesian friends in Gothenburg, thank you for all valuable help during my stay in Sweden which made me feel really like at home.

My mother and **my father** for providing me with the opportunity to be where I am today. I love you so much. Also, for my sister, **Mbak Dama**, who supported me and helped me throughout my life.

The ultimate thanks are contributed to the most important people in my life now. For my daughter, **Khaylila**, and the newest member in Nugraha's team, **Faruq**, thank you for making me stronger, better and more fulfilled than I could have ever imagined. I love you to the moon and back. For my beloved wife, **Anggi**, I love you for everything, for being so understanding and for putting up with me through the toughest moments of my life. You are the best thing that has ever happened to me.

List of Abbreviations

BC	Boundary Condition
CFD	Computational Fluid Dynamics
DPM	Discrete Particle Model
DRW	Discrete Random Walk
EDC	Eddy Dissipation Concept
EDM	Eddy Dissipation Model
EU	European Union
FRK	Finite-rate Kinetics
LCV	Low Calorific Value
LPG	Liquiefied Petroleoum Gas
ODE	Ordinary Differential Equation
PAH	Polyaromatic Hydrocarbon
PDE	Partial Differential Equation
PM	Particulate Matter
RTD	Residence Time Distribution
SEM	Scanning Electron Microscopy
UDF	User-defined Function

TABLE OF CONTENTS

1. Introduction

1.1. Background

The increase of the greenhouse effect, as well as the depletion of fossil fuels, has sparked global interest in the use of increasingly renewable and eco-friendly energy sources [1]. Biomass as an alternative energy source is seen as one of the global solutions to the aforementioned issue. The vast resource of biomass energy, which has been reported as the world's fourth largest energy source, demonstrates its significant potential to be further exploited [2]. This global awareness has driven biomass energy sources used to meet renewable energy utilization targets for some regions and countries, such as the EU, which is set to be 27% in 2030 [3], and Sweden, which is set to be 100% in 2040 [4] (% renewable energy from total energy production).

Different mechanisms, including direct combustion, thermochemical, chemical, and biological conversion, might be used to convert biomass into thermal and chemical energy. Among various conversion mechanisms, biomass combustion is regarded as one of the most popular and simple methods of converting energy from biomass, which might be utilized immediately for building and water heating, industrial process heat, and electricity generation through steam turbines [5]. Nevertheless, biomass combustion is a major cause of particulate matter (PM) air pollution in the outdoors [12]. Biomass combustion produced approximately 20% of total $PM_{2.5}$ emissions in the United States and China [6,7]. While domestic biomass combustion contributed up to 70% of total organic PM in the air during the winter season in Europe [8].

Particulate matter is a harmful substance for both humans and the environment. It is estimated that particulate matter pollution in the air caused around 4.2 million premature mortalities in 2016 [9]. Furthermore, particulate matter from biomass combustion adds to climate change by absorbing and dispersing sunlight. The carbonaceous molecule in PM has been shown to absorb sunlight, contributing to more severe global warming. PM emissions have also been proven to impact cloud formation, which has an indirect effect on climate change [13]. As a result, decreasing PM from discharged flue gas in biomass combustion systems has attracted the scientific and industrial communities' attention in recent decades.

In recent years, particulate matter emission reduction methods in the biomass combustion sector have focused on combustion process optimization and flue gas cleaning [10]. The efficacy of both reduction measures is dependent on the availability of PM characteristics information. A thorough understanding of how PM is created and reduced in the combustion system might provide a significant advantage in determining the appropriate reduction strategy. PM formation and removal are well-studied phenomena, although they remain an active focus of research today [11]. This is owing to the intricacy of the PM formation pathway, which is influenced by several combustion factors, including parent fuel properties (size and chemical compositions) and combustion conditions (the mixing of air and fuel, the air fuel ratio, combustion temperature and gas residence time). Despite several studies conducted, identifying a valid scheme for PM formation and reduction in biomass combustion is challenging because of the broad range of these factors [12].

PM formation and reduction in combustion systems are now being investigated in gasoline engines [13-16], diesel engines [17-22], and coal combustion systems [23-31]. In other combustion systems, combining experimental and CFD simulation studies has resulted in a better understanding of PM formation and reduction. As a result, it is believed that the development of CFD modelling methods that are extensively validated using accurate experimental data could speed the understanding of PM formation and constitute a step toward PM reduction in biomass combustion systems.

CFD modelling of the combustion system may include biomass particle models. A precise physicochemical particle model is required to anticipate the right PM precursor release, resulting in a more accurate prediction of the PM formation pathway. To be implemented, the particle model must also be stable and computationally efficient [32,33]. The precise and efficient particle model could be employed on higher simulation scales, such as in the biomass furnace, where the simulation should properly predict the combustion behavior as found in reliable experimental data. The comparison of modelling and experimental values should be done thoroughly, taking into account the many different combustion parameters that are crucial for PM mitigation, such as residence time, temperature, stoichiometry level, and mixing condition [34].

A successful model allows different level of operating conditions in the reactor to be evaluated by computer simulation, which may significantly reduce the number of costly experiments. Finally, simulation approaches may be useful in determining the optimal biomass combustion condition with the lowest PM emission in a more precise and efficient manner.

1.2. Objectives

Based on the problems outlined in the Background section, the primary goal of the PhD research is to get a better understanding of PM formation and reduction in biomass combustion systems. The knowledge development consisted of experimental, and simulation works on different scale which has been also thoroughly presented in the four different scientific articles.

To support the primary objective, the current effort has included the development of a biomass particle model. The model should be able to accurately predict particle combustion behavior and, as a result, PM precursor release. The particle model must also be stable for a variety of particle properties and combustion conditions. The developed model must be sufficient to allow further implementation in a larger scale simulation and CFD analysis framework. This work has been thoroughly explored in **Paper I** and **II**. The formulated particle model in these papers were utilized further to support sub-grid scale biomass combustion simulation in the furnace.

Papers III and **IV** investigated the design and construction of an advanced research-scale biomass combustion furnace, as well as the formulation of an experimental approach for observing PM formation and reduction in a biomass combustion system. The furnace should allow for the flexible modification of a combustion setup, such as gas residence time in the furnace, supplied air temperature, and varied mixing conditions, by modifying combustion stoichiometric condition and secondary air injection. The furnace should also enable precise, flexible, and real-time measurement of key combustion parameters such as temperature,

exhaust gas composition, and particle properties (concentration, composition, morphology, and size distribution).

The larger simulation scale, i.e., the CFD simulation to predict the observed combustion behavior, was also formulated in **Papers III** and **IV**. These articles presented a steady CFD analysis that was later improved into a time-resolved CFD analysis. Full-scale combustion simulations enable the quantification of global and instantaneous profiles of combustion parameters. The correct prediction of gas composition and temperature distribution, as well as gas residence time in the furnace, are critical in predicting PM emissions.

1.3. Outline

This thesis is presented as follow:

Chapter 2 is devoted to a discussion of the phases of biomass combustion, with a specific emphasis on the relationship between these stages and PM formation and reduction. This chapter also includes a description of standard modelling approaches for biomass decomposition stages, combustion in the gas phase, and the formation and reduction of PM.

Chapter 3 describes the development of the experimental furnace, the experimental method, and the key findings from the experimental campaign. This chapter also includes a detailed discussion of the accuracy of data sampling.

Chapter 4 discusses the construction and results of single particle mathematical modelling and simulation. This comprises heat and mass balance in a single particle system, as well as the Stefan flow effect on heat and mass balance. This chapter also emphasizes the significance of developing an accurate and efficient particle model that will be utilized in multi-particle simulations, such as those used in biomass furnaces.

Chapter 5 is devoted to the formulation and discussion of the major findings of CFD simulation in a biomass combustion furnace. This chapter presents and compares two modes of CFD simulation: steady and transient. CFD simulation accuracy is compared against experimental results. The quantitative and qualitative evaluation of PM formation and reduction during biomass combustion is based on the results of CFD simulation and experimental studies.

Chapter 6 highlights the key findings of this study and offers a recommendation for further research.

2. Biomass Combustion and Particulate Matter Emission

2.1. Biomass combustion mechanism

2.1.1. Drying

Water exists as bound water, free water, and water vapor in the biomass matrix. Water is taken up as bound water until all accessible adsorption sites are occupied, at which point it becomes free water and fills the pores of the biomass [35]. Capillary forces and diffusion generated by concentration gradients allow free and bound water to move within the particles. Free water and bound water have distinctive characteristics in terms of movement and evaporation. As a result, these two distinct types of water must be handled with care [36].

In the literature, the drying process is represented using three main approaches: equilibrium, a heat sink (thermal drying), and Arrhenius (kinetics) models [37,38]. Equilibrium models are extensively used to predict low-temperature drying, such as the drying of wood for construction materials. The step function of evaporation is used in the heat sink model, which might cause numerical instability. Due to its broad temperature range and high numerical stability, the kinetics model is widely used. Both of these enhance the stability and accuracy of models of fast drying conditions, particularly in high-temperature environments, such as biomass drying in a high-temperature furnace [39].

2.1.2. Devolatilization

Pyrolysis and devolatilization are terms that are used interchangeably to describe the thermochemical degradation of biomass in the absence of an oxidizer [36]. Biomass begins to devolatilize at higher temperatures than water drying, i.e., over 350^{o}C, and it may proceed in stages, i.e., primary and secondary devolatilization, with multiple parallel and consecutive reactions occurring. The formation and release of pyrolytic gases and solid char are part of the primary stage. [40]. Pyrolytic gases are often divided into two components: volatile gas and tar. A volatile gas is a gas mixture made up of lighter gas molecules than tar molecules, e.g., CO_2, CO, H_2, H_2O, CH_4, C_2H_4, and C_2H_2 [41]. Tar is commonly characterized as a mixture of larger hydrocarbon molecules such as C_6H_6, C_6H_6O, $C_{10}H_8$, C_7H_8 [11,42]. Secondary devolatilization happens during primary tar outbound movement. Primary tars participate in a variety of complex reactions during this stage, including cracking, reforming, dehydration, condensation, polymerization, oxidation, and gasification [43].

The Arrhenius reaction kinetic form is commonly used to simulate biomass devolatilization. In the literature, various reaction schemes with varying degrees of complexity and accuracy have been presented. The main distinction is if biomass is considered to be a single compound [33,35,44–49] or divided into three lignocellulosic components, namely cellulose, hemicellulose, and lignin [50–52]. The single compound assumption leads to a simpler devolatilization scheme, as shown in Figure 1a and b, which include the global single reaction and the competitive reaction models.

The inclusion of lignocellulosic components to simulate biomass decomposition is proposed to follow the single and dual routes process as depicted in Figure 1c and d. The use of different lignocellulosic compounds may allow for a more accurate prediction of soot formation, as it was found to be primarily affected by lignin devolatilization [53–55]. Based on various experimental observations during flash pyrolysis [56,57], the inclusion of active compound in Figure 1d is considered to be more accurate model compared to the model with the absence of active compound [58]. Furthermore, the mechanism shown in Figure 1d is also found to have wide range application for different cellulose, hemicellulose, and lignin compositions in biomass i.e., from ±17% to 50% of each compound [59].

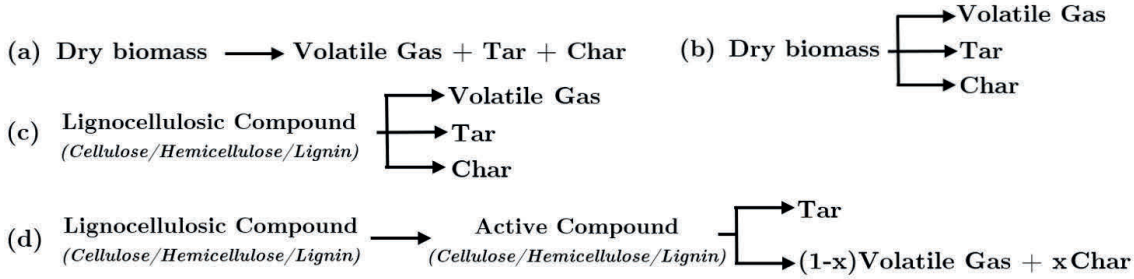

Figure 1. Different biomass devolatilization schemes.

2.1.3. Char combustion

The char produced by biomass devolatilization participate in heterogeneous char reaction, which includes the interaction of remaining solid carbon (char) with oxidative gases. A set of transport mechanisms and chemical reactions control the char conversion rate [60]. These include 1) film diffusion of an oxidizing compound, 2) diffusion through the ash layer and particle, 3) adsorption onto the reaction surface, 4) chemical reaction, 5) desorption of product gas from the surface, 6) diffusion of product gas through the particle and the ash layer, and 7) film diffusion back into the ambient gas. Except for the chemical reaction (step number 4), the remaining steps are mass transport. Based on Thiele modulus (the ratio of overall reaction rate to diffusion rate) and effectiveness factor [61], there can be three distinct regimes of char conversion in a system, depending on whether the reaction occurs inside the particle, at the particle surface, or both. The balance between mass transfer and reaction rates, which is significantly influenced by temperature, is the most influential factor in determining reaction location [61]. Exothermic combustion rapidly raises the surface temperature after ignition, and the process becomes mass transfer limited for the majority of the time.

The simplification of char oxidation and gasification reactions, as shown in the reaction scheme below, is widely used [36].

$$C + O_2 \rightarrow CO_2$$
$$C + CO_2 \rightarrow 2\,CO$$
$$C + H_2O \rightarrow CO + H_2$$

2.1.4. Gas phase combustion

Gas phase combustion is the oxidation of volatiles in the presence of an oxidant, such as oxygen. The gas phase reaction pathway is determined by the amount and composition of

volatile species. During the devolatilization stage, biomass is converted into pyrolytic gas, which consists of several small molecules e.g., CO_2, CO, H_2, H_2O, CH_4, C_2H_4, and C_2H_2 [41], and larger hydrocarbon molecules, usually referred to as tar. The simulation accuracy of pollutant formation is dictated by the accuracy of volatile species introduced from devolatilization and their composition.

One of the key issues in development of biomass combustion models is accurate prediction of biomass devolatilization products. Several earlier studies used a common approach based on global energy and mass balance, which has been shown to provide good agreement with experimental observations in a wide range of biomass samples [62,63]. Some previous studies have also shown a development based on an advanced chemical percolation devolatilization model (CPD) [64]. Various prior studies have used data from coal pyrolysis systems to predict the pyrolysis product of biomass combustion [65,66]. The major challenge with this model is that it has not been validated for a large variety of biomass samples [67].

In computational fluid dynamics analysis framework, gas phase reaction in biomass combustion system is commonly modelled using species transport models i.e., finite-rate kinetic/ eddy dissipation model (FRK/EDM) [68,69] and eddy dissipation concept (EDC) [70–73]. The FRK/EDM model computes mixing and kinetic reaction rates at each cell, and the combustion rate is determined by the lowest value of both. This model does not take into account the detailed chemistry of reactions under mixing-limited condition. As a result, predicting pollutants such as CO, NOx, and intermediate species remains as a challenge in the FRK/EDM model [74].

The eddy dissipation concept (EDC) model proposed by Magnussen [75] provides the capacity to incorporate specific chemical reactions required for prediction of pollutant formation. In EDC, the reactions occur in so-called fine structures, and the rate of the reaction is controlled by mass transfer between the fine structures and the surrounding gas [73]. This model was developed primarily for highly turbulent flow conditions to compensate for the interaction of turbulence and detailed reaction kinetics [72]. Therefore, the main drawback of the EDC model is inapplicability to predict accurate temperature and gas species composition in considerable low turbulent flow [76].

2.2. Particulate matter formation and reduction

2.2.1. Origin of particulate matters

Particulate emissions from biomass burning include particles with varying chemical compositions that may be classified as inorganic ash particles, organic carbon particles, and soot (elemental carbon agglomerates) [77]. These various particles are produced by different phenomena within the combustion chamber. In summary, inorganic ash particles are formed from inorganic elements that vaporize during combustion. These inorganic vapors nucleate as the flue gas cools, forming ultra-fine particles that can grow by coagulation and condensation. Incomplete combustion produces both soot particles and organic carbon particles. Organic materials in the particulate matter are formed by unburned condensed organic vapor produced during the devolatilization stage [78]. Condensation may occur at a colder place, such as near the chimney.

In contrast to organic material, soot particles are generated inside the fuel-rich area of the flame by complex mechanism from tar, PAC, and small molecules such as acetylene (C_2H_2) [79]. These mechanisms include the formation of soot nuclei from gaseous hydrocarbons which is followed by particle growth due to surface reactions, coagulation, and agglomeration [80]. A soot particle can be oxidized in the oxygen-rich region of the flame under optimum combustion condition. The conceptual route for the formation of particulate matter from these three components is shown in Figure 2.

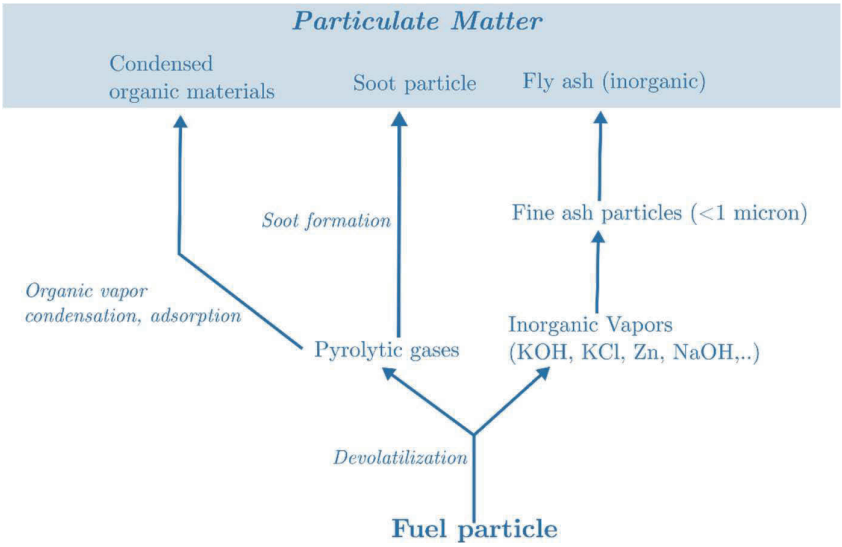

Figure 2. PM formation in biomass combustion, adapted from Sippula et al. [81].

2.2.2. Soot emission modelling

The soot formation and reduction modelling has been extensively developed for gasoline, diesel, and liquid and gaseous fuel systems. The same model as used in combustion engines was commonly applied to model soot production in biomass combustion systems. It does, however, require information on the first precursors for soot production that were produced during the devolatilization stage [11,42].

There are several models for soot formation and reduction available, which generally can be classified into three categories [82] i.e., empirical, semi-empirical and detailed chemistry models. One of the most widely used empirical models is the one-step Khan and Greeves model [83]. It assumes that the formation of soot particles, i.e., the soot inception rate, controls the soot formation process and ignores the precursors' stage. The empirical soot formation rate is calculated as a function of pressure, unburned gas equivalency ratio, and temperature [83]. In contrast to a model governed by a correlation derived from experimental data, the semi-empirical model attempts to combine some physical and chemistry aspects. This usually leads to the development of rate equations for reactions of soot precursors and soot particles with a simple description of the chemistry, as proposed by one of semi-empirical models i.e., the two-step Tesner model [84].

The more detailed models introduce more complex chemistry and uses less empirical correlation as have been developed by several researchers e.g., Moss-Brookes [85], Moss-Brookes-Hall [86] and Method of Moments models [87]. These three models account for

various physical and chemical phenomena that occur in soot formation and soot particle evolution, such as nucleation, coagulation, surface growth, and oxidation. The second model extends the previous model's applicability to work not just for methane systems, but also for heavier hydrocarbon systems. In contrast to the first two models, which do not take particle size distribution into account, the Method of Moments model predicts soot formation using the soot particle population balance method. It takes into consideration soot size distribution, where the diameters of soot particles change dynamically throughout the combustion chamber.

3. Experimental Studies

3.1. Experimental facility

A fixed grate-fired furnace as shown in Figure 3, was designed and built to investigate the behavior of biomass combustion further. **Paper III** presents in detail the experimental conditions utilized in the current work.

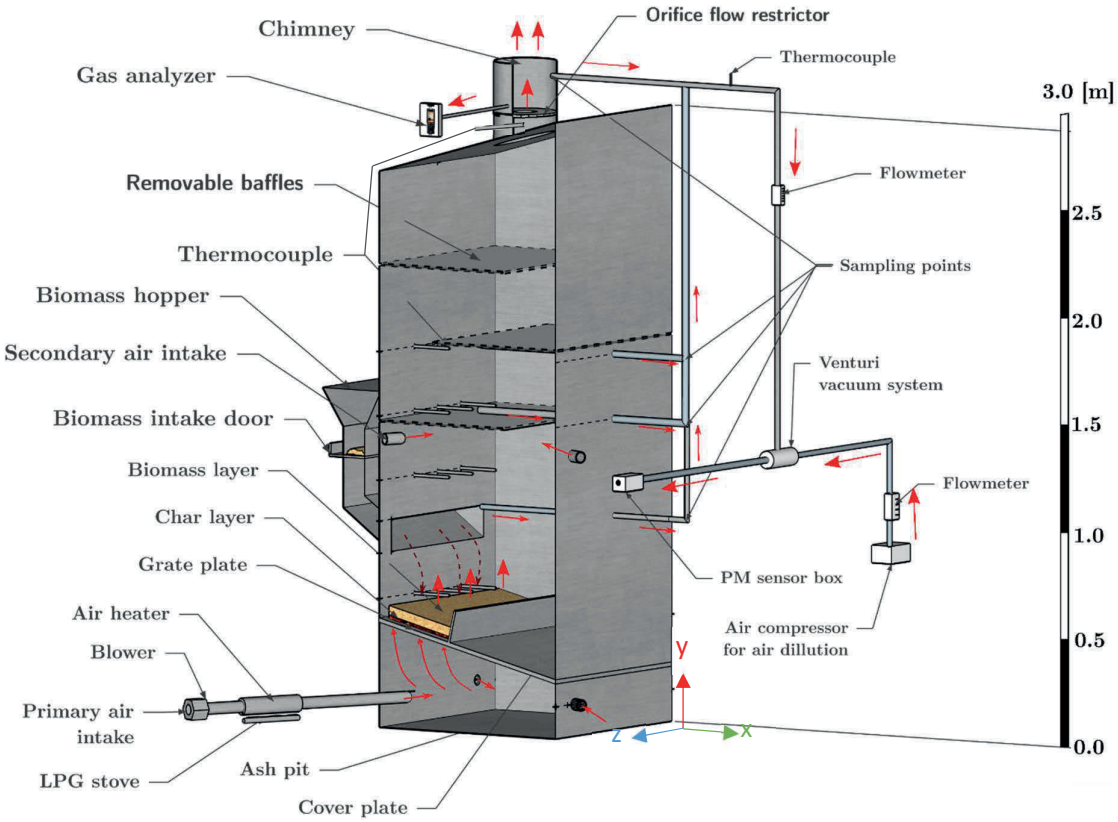

Figure 3. Schematic view of the grate-fired furnace (red arrows indicate the gas flow and dashed brown arrows show the biomass movement).

The biomass is fed into the grate through a hopper, and primary air is introduced into the furnace from the bottom of the grate by a blower. A 13 cm orifice flow restrictor is installed in the chimney to reduce air leakage into the furnace. Nevertheless, based on the comparison of air flow rate measurement and oxygen measurement at the chimney, around 15% of air leakage was still recorded. To minimize heat loss through the walls, 25 cm of insulation was added to the furnace wall.

Type K thermocouples measure the gas temperature in the freeboard and are connected to a DataTaker DT85 (Thermo Fisher Scientific, Australia) for data acquisition. The two thermocouples method [88] is used in the present work to improve the accuracy of the gas temperature measurement. The gas temperature is calculated using Eq. (1), which is derived from the thermocouple's steady-state energy balance equation for smaller and bigger

thermocouples as shown in Eq.(2). Here, subscript l, indicates the larger diameter thermocouple and subscript s represents the smaller diameter thermocouple.

$$h\left(T_g - T_b\right) = \varepsilon_b \sigma (T_b^4 - T_\infty^4) \quad (1)$$

$$T_g = \frac{\varepsilon_b \sigma (T_{b,s}^2 + T_{b,l}^2)(T_{b,s} + T_{b,l})(T_{b,s} - T_{b,l})}{h_s - h_l} + \frac{h_s (T_{b,s} - T_{b,l})}{h_s - h_l} + T_{b,l} \quad (2)$$

A Kane 457 gas analyzer was used to record the CO_2 composition of the exhaust stream (Kane International Limited, England). This infrared CO_2 sensor has a 0.1vol% resolution, a 20 s response time, and a ±0.3vol% accuracy.

The PM concentration is measured using SDS011 (Shandong Nova Fitness Co.Ltd., China), which monitors particles as small as 0.3 μm and provides $PM_{2.5}$ and PM_{10} concentration values. The working principle of SDS011 is based on optical light scattering i.e., particles flow through the sensor inlet and are channeled through a laser beam [89]. SDS011 can measure PM concentrations as high as 999.9 mg/m^3 for $PM_{2.5}$ and 1999.9 mg/m^3 for PM_{10} with a maximum relative error of measurements up to ± 15% [90].

Gravimetric analysis was also performed to validate the PM sensor value. To trap the PM particles, a Particulate Respirator Filter 8210, N95 160 EA/Case from (3M, United States) was used. This filter captures 95% of all particles larger than 0.3 μm in size [91,92]. During the sampling period, the filter with its adaptor was placed in the PM trapping system. Following that, the moisture content in the filter was removed by drying it in an oven at 90°C for 5 hours. Furthermore, the PM deposited on the filter was examined using SEM using an FEI Quanta 650 Scanning Electron Microscopy (SEM) (Thermo Fisher Scientific, United States) [93].

The furnace design incorporates the following characteristics to better understand the impact of different operating conditions on PM emissions:

- Baffle(s) in the freeboard that may be installed/removed to change the gas residence time.
- Adjustable primary and secondary air flow rates.
- Adjustable primary air pre-heating.
- Multiple on-line PM sampling points located at 100 cm, 145 cm, 175 cm, and 325 cm (at the chimney) from the ash pit.

3.2. Experimental design

The coconut shell was chosen for this study because it has significant potential as a renewable energy source, not only because of its high energy content (16-18 MJ/kg), but as well as because it is a plentiful resource, particularly in tropical countries. Coconut shells were crushed into 5x5 cm up to 10x10 cm size before it was used in combustion experiment. The current biomass's proximate and ultimate analysis is summarized in Table 1.

Table 1. Ultimate and proximate analysis results (%adb)*.

Ultimate Analysis (%mass)				Proximate Analysis (%mass)			
Carbon	**Hydrogen**	**Oxygen**	**Nitrogen**	**Volatile**	**Ash**	**Fixed Carbon**	**Moisture**
47.5	6.23	45.47	0.11	72.4	0.6	19.4	7.6

* adb: air dried basis or without free moisture content

The combustion experiment began with the furnace heating up with an LPG heater and continued with reloading 1 kg of biomass every 3 minutes until steady state operation was obtained, as shown by constant average thermocouple readings from one biomass reloading to another. Then, the specific biomass feed rate, 20 kg biomass per hour, was reloaded 1/60 every minute i.e., 1/3 kg/minute, until the end of the experiments. The graphs in Figure 4 and Figure 5 depict the evolution of chimney temperature during the various stages of combustion.

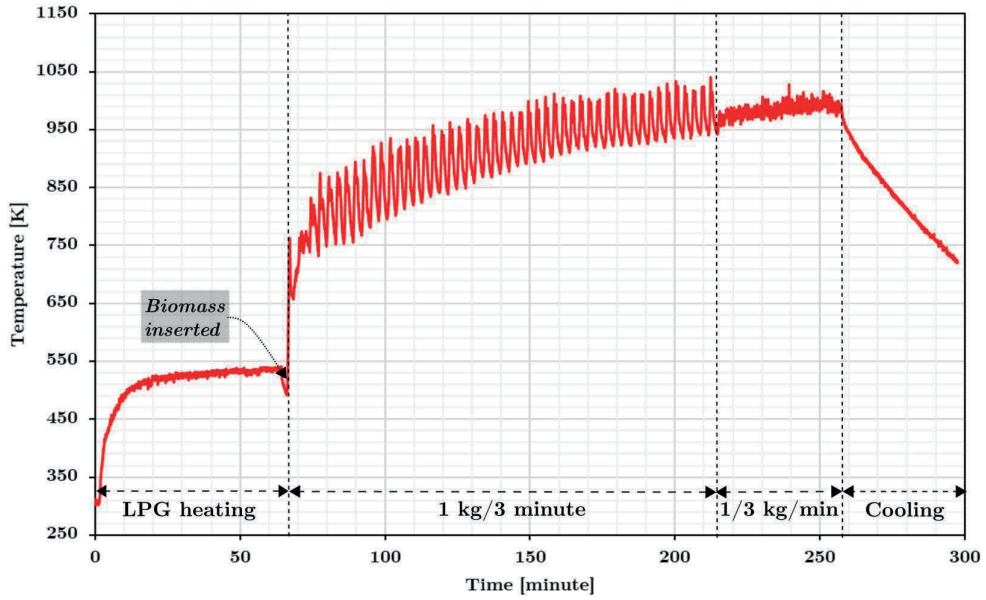

Figure 4. Temperature profile in the chimney during different combustion stages.

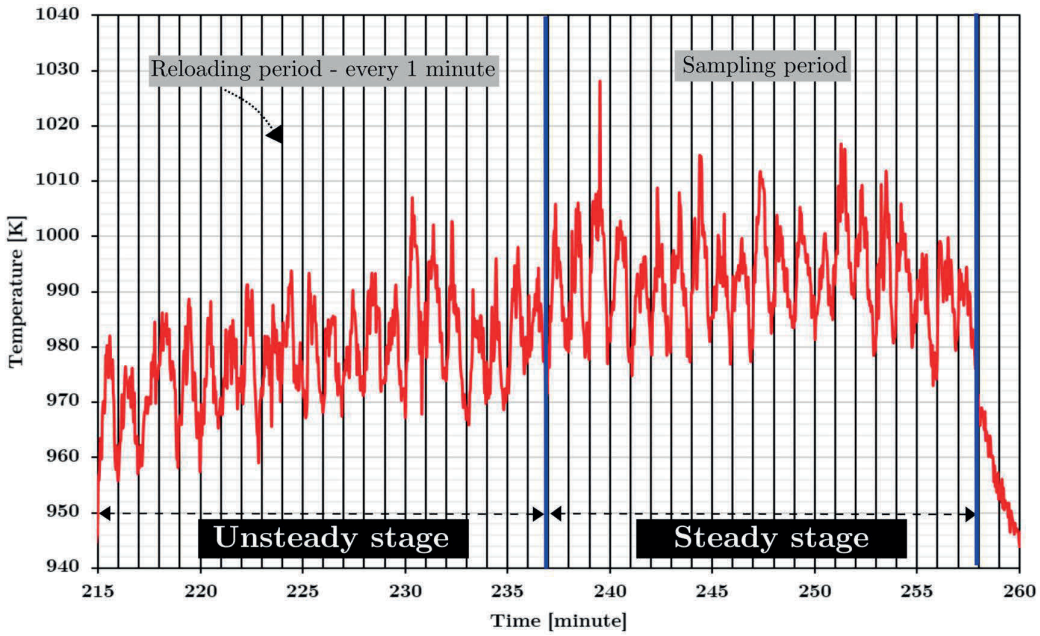

Figure 5. Temperature profile in the chimney during 1/3 kg per minute reloading frequency.

During the steady-state operation, all combustion parameters, such as gas composition using a gas analyzer and PM concentration using a PM sensor and a PM filter, were recorded. The typical PM and CO_2 signal from sensor measurement throughout the sampling time is shown in Figure 6. The accumulated char was monitored after the final biomass was fed, i.e., during the cooling stage, by integration of the CO_2 concentration at the outflow until no CO_2 was recorded. Because the sample gas from the furnace was diluted with air from the compressor in the venturi, the PM signal from the sensor must be normalized. During the sample period, an air-to-gas volume ratio of 50:1 was maintained in the PM sampling system.

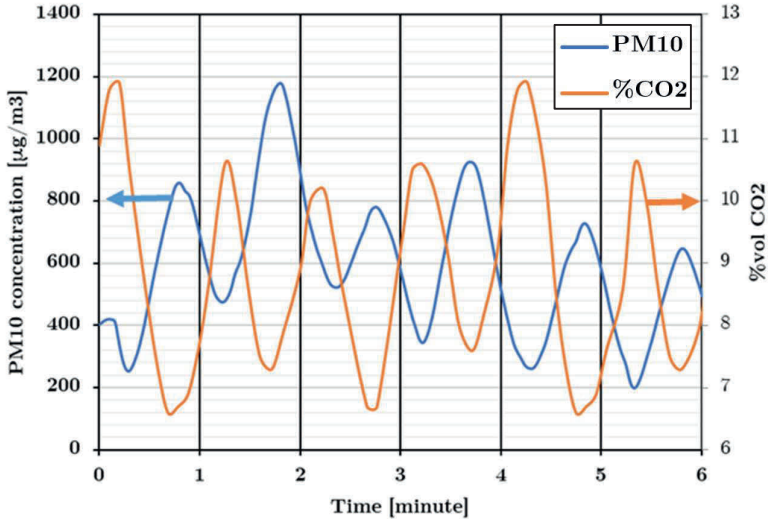

Figure 6. PM_{10} and CO_2 concentration measurements at the chimney during sampling period.

Several operating conditions were investigated to obtain information about PM emissions from the combustion system. The amount of particulate matter (PM) in exhaust gases is affected by residence time, temperature, and oxygen concentration within the furnace [94]. Consequently, the experimental design of the current work consists of the following operating conditions:

1. Gas residence time (furnace with and without baffles installed)
2. Air preheating temperature (using LPG fueled air preheater)
3. Different stoichiometric condition (by varying excess air level)

Additional operating conditions explored to assess the measurement sensitivity include:

4. Biomass sizes
5. Biomass distribution on top of the grate

The current work includes experiments at eight different operating conditions, including different furnace designs. Each experiment includes 5-10 biomass re-loadings, and the various experiments and corresponding operating conditions are summarized in Table 2 and Table 3.

Table 2. Operating conditions in the main experimental plan.

Experiment ID	% Excess air	Air temperature (°C)	Baffle	Number of repeated experiments	Total number of measurement data
Exp 1	90	30	No	5	35
Exp 2	90	70	No	3	22
Exp 3	80	30	No	2	12
Exp 4	90	30	Yes	2	14
Exp 5	90	75	Yes	2	14

Table 3. Supplementary experiments to assess measurement sensitivity.

Experiment ID	Biomass size (cm)	Biomass distribution	Number of repeated experiments	Total number of measurement data
Exp 6	4	Uniform	1	10
Exp 7	7	Uniform	1	8
Exp 8	5-10	Centered	1	5

*all experiments in Table 2 use 90% excess air, no baffle, and primary air at 30°C.

3.3. Convolution method

Both the CO_2 gas analyzer and PM sampling system are considered as a non-ideal plug-flow system. Therefore, it is important to account for the hydrodynamic dispersion that occurs inside the piping systems and sensors when comparing the CFD results with the experimental observations. The CFD result should be convoluted by the residence time distribution (RTD) for the specific measurement system.

The residence time distribution (RTD) inside the respective sampling system was determined using step response experiments with constant CO_2 and PM sources. The sampling probe was attached to the constant source and maintained for several minutes to ensure that the sensor's reading value remained constant. The tracer's RTD during the step response experiment is given by Eq (3). The final RTD curve from the CO_2 and PM sampling systems is shown in Figure 7. The RTD is then used to convolute the result obtained by CFD simulation using the built-in function *conv* in Matlab 2018b (The MathWorks, USA).

$$E(t) = \frac{C(t)}{\int_0^\infty C(t)\,dt} \tag{3}$$

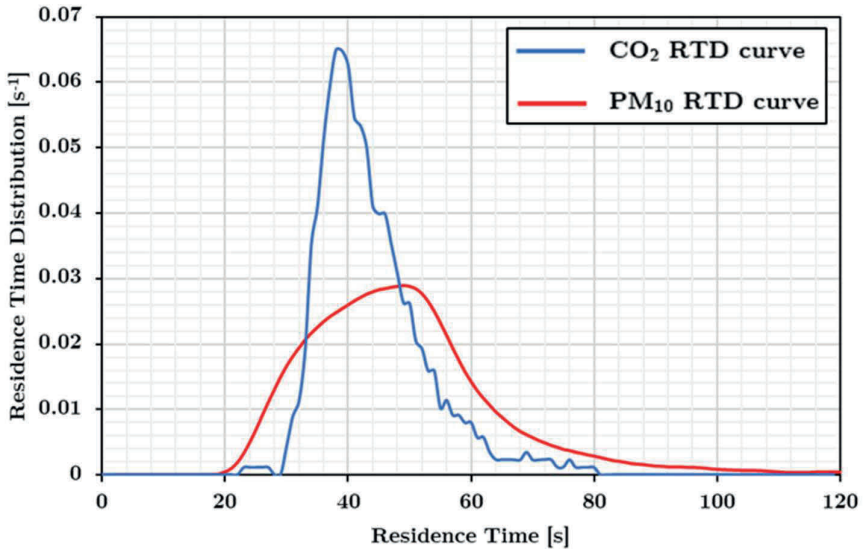

Figure 7. The residence time distribution of PM_{10} and CO_2 in the respective sampling system.

3.4. PM measurements

3.4.1. Accuracy of PM sensor

The accuracy of the PM sensor was evaluated by comparison with results from gravimetric analysis. A comparison from three different locations in the furnace is shown in Figure 8. For the three different sample locations, the ratio between the gravimetric analysis to PM sensor was 1.45, 1.88, and 1.55. These numbers are consistent with the results of Schwarz, A.D., et al [89], which showed that gravimetric analysis produces 1.56 times higher PM concentration than the PM sensor. This signifies the precision of the current sample system to be used for measuring PM concentrations.

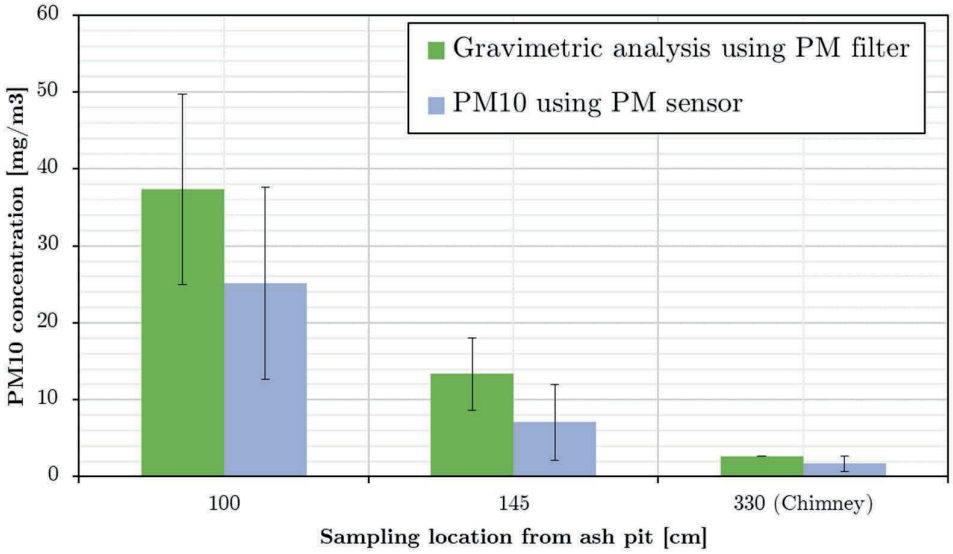

Figure 8. Comparison between PM filter N95 and PM sensor SDS011 at different sampling locations inside the furnace.

3.4.2. PM morphology

SEM analysis reveals the presence of both individual particles and particle agglomerates on the filter. After a sufficiently significant loading, a PM cake can form on the filter's top layer. The SEM result confirm the ability of PM sensor to measure PM concentration in the biomass combustion system since the particles are observed to be averagely 1 µm in size.

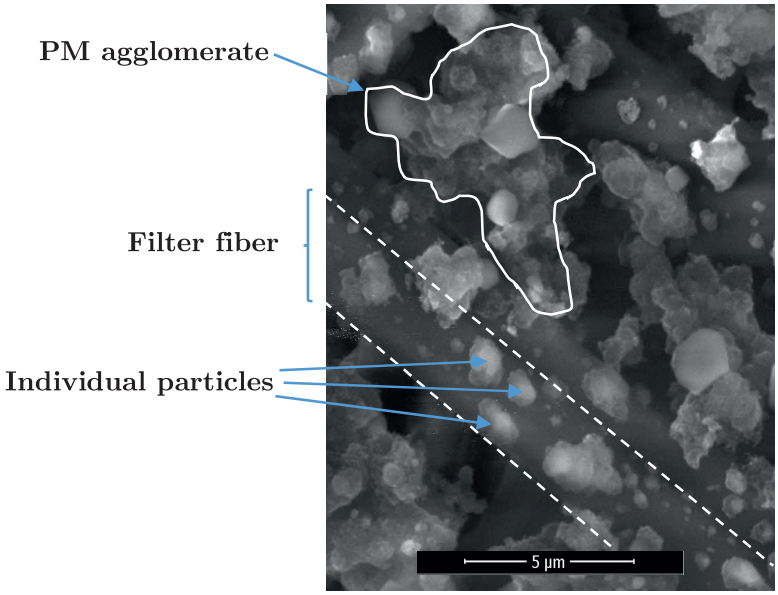

Figure 9. SEM result of PM collected on the filter for Exp1 at 325 cm (chimney) measurement position

3.4.3. Sensitivity of PM measurement

The PM_{10} concentration is highly sensitive to how the biomass particles are distributed over the grate as reported in Figure 10. Poor mixing of flue gas and air, as well as an unfavorable air/fuel ratio, are seen to cause higher PM concentrations in the centered pile of biomass (Exp9) experiment compared to the uniformly distributed biomass. Meanwhile, biomass sizes are shown to have no significant effect on the final PM_{10} concentration in the range of examined conditions.

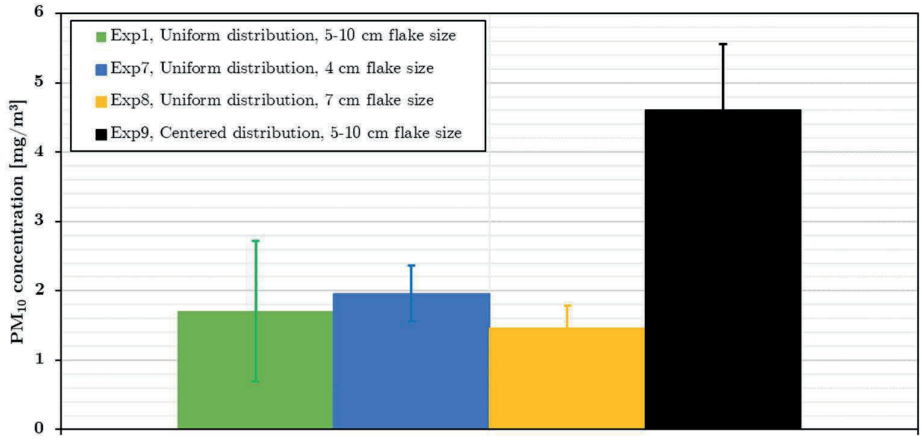

Figure 10. Average PM_{10} concentration and standard deviations in the chimney for supplementary experiments.

4. Single Particle Modelling and Simulation Studies

4.1. Model formulation for biomass particle pyrolysis and combustion

The particle model is developed by taking into account the model's ability to handle important physicochemical phenomena in biomass pyrolysis and combustion, such as arbitrary reaction kinetics, local varying material properties, heat adsorption by evaporated gas, gradient-driven transport mechanisms such as water movement by diffusion inside the biomass matrix, and inclusion of the effect of Stefan flow on the heat and mass transfer rates at the particle surface. The 1D transient particle model is formulated as described in the next sub-section.

4.1.1. Heat and mass balance

The global energy conservation equation for 1D transient simulation follows Eq. (4).

$$\sum \rho_k Cp_k \frac{\partial T}{\partial t} = \frac{1}{r^a}\frac{\partial}{\partial r}\left(r^a \lambda_{eff}\right)\frac{\partial T}{\partial r} - \dot{r}_{v,g}\, Cp_g \frac{V_p}{A_p}\frac{\partial T}{\partial r} + \left(D_{fw} Cp_{fw}\frac{d\rho_{fw}}{dr} + D_{bw} Cp_{bw}\frac{d\rho_{bw}}{dr}\right)\frac{dT}{dr} - \Delta H_{dry}\dot{r}_{v,dry} - \Delta H_{dev}\dot{r}_{v,dev} \quad (4)$$

Here superscript a depends on the biomass geometry (0 for planar, 1 for cylinder, and 2 for sphere). The term on the left side of Eq.(4) shows the accumulation term. The boundary condition for the heat balance at the particle surface follows Eq.(5). Heat conduction into the particle is balanced by heat transfer from or to the particle's surroundings by convection and radiation, as well as heat from the char reaction at the particle surface.

$$\lambda_{eff}\frac{\partial T}{\partial r} = h_{eff}\left(T_{bulk} - T_{surf}\right) - \sigma\omega\left({T_{surf}}^4 - {T_{wall}}^4\right) - \Delta H_{char}\dot{r}_{s,char} \quad (5)$$

Eqs.(6) to (9) explain the mass evolution of dry wood, free water, char, and bound water. The density adjustment due to particle shrinkage and swelling is taken into account in the last term on the right side of each equation. The gradient of free and bound water drives the water movement via diffusion, and this physical phenomenon is accounted for in the first term on the right-hand side of Eqs.(7),(8) and (9).

$$\frac{\partial \rho_b}{\partial t} = -\dot{r}_{v,dev} - \frac{\rho_b}{V}\frac{dV}{dt} \quad (6)$$

$$\frac{\partial \rho_{fw}}{\partial t} = \frac{1}{r^a}\frac{\partial}{\partial r}\left(r^a D_{fw}\right)\frac{\partial \rho_{fw}}{\partial r} - k_4\,\rho_{fw} - \frac{\rho_{fw}}{V}\frac{dV}{dt} \quad (7)$$

$$\frac{\partial \rho_c}{\partial t} = k_3\,\rho_b - \frac{\rho_c}{V}\frac{dV}{dt} \quad (8)$$

$$\frac{\partial \rho_{bw}}{\partial t} = \frac{1}{r^a}\frac{\partial}{\partial r}\left(r^a D_{bw}\right)\frac{\partial \rho_{bw}}{\partial r} - k_5\,\rho_{bw} - \frac{\rho_{bw}}{V}\frac{dV}{dt} \quad (9)$$

The porosity evolution inside biomass is expressed in Eq.(10).

$$\frac{\partial \varepsilon}{\partial t} = -\left(\frac{\partial \rho_b}{\partial t} + \frac{\partial \rho_c}{\partial t} + \frac{\partial \rho_{fw}}{\partial t} + \frac{\partial \rho_{bw}}{\partial t}\right)\times\frac{(1-\varepsilon)}{\rho_{tot}} + \frac{(1-\varepsilon)}{V}\frac{dV}{dt} \quad (10)$$

The volume change caused by shrinking and swelling during drying, pyrolysis, char gasification, and oxidation is given by Eq.(11).

$$\frac{dV}{dt} = \frac{V_0(\beta_m - 1)}{\rho_{fw_0} + \rho_{bw_0}} \dot{r}_{v,dry} + \frac{V_0(\beta_b - 1)}{\rho_{b_0}} \dot{r}_{v,dev} + \frac{A_p \dot{r}_{s,char}}{\rho_{tot}} \quad (11)$$

β_m and β_b are the swelling or shrinking parameters for drying and devolatilization. Table 3 in **Paper I** summarizes the supporting equations for heat and mass balances. Due to the influence of Stefan flow, the nominal Nusselt and Sherwood numbers need to be modified to predict the correct rate of heat and mass transfer to the particle. Table 4 in **Paper I** summarizes the nominal Nusselt and Sherwood numbers before the correction due to Stefan flow for various particle geometries

The following assumptions are made in the current simulations:

1) Gas behaves as ideal gas.
2) Secondary devolatilization is not considered.
3) Solid biomass is in local thermal equilibrium with the evaporated gas.
4) Particle shrinking only occurs at the char reaction stage. The exclusion of particle shrinking and swelling during drying and pyrolysis is due to the lack of evidence of particle volume changes during drying and devolatilization in the experimental data used for validation [36].
5) Char oxidation and gasification only occur at the particle surface.
6) The ash layer has high permeability due to the significant Stefan flow rate.
7) Due to the low density of gas in comparison to the solid biomass, the heat capacity of gas in the accumulation term is neglected.

The particle model that has been formulated was subsequently used to simulate the pyrolysis and combustion of poplar wood particles as listed in Table 4 as Case A to D. The kinetic rate data has been summarized in Table C.2. in **Paper I**.

Table 4. Experimental conditions from Lu et al.[36].

Experiment condition	Case A	Case B	Case C	Case D
Wall temperature (K)	1276	1276	1276	1276
Gas temperature (K)	1050	1050	1050	1050
Initial moisture content (wt%)	6	6	40	40
Gas material	Nitrogen	Nitrogen	Nitrogen	Air
Particle shape	Sphere	Cylinder	Cylinder	Sphere
Particle material	Poplar	Poplar	Poplar	Poplar
Particle diameter (mm)	9.5	9.5	9.5	9.5

4.1.2. Orthogonal collocation particle discretization

In modelling thermally thick particles, the non-uniformity of temperature is expected to be significant. As a result, a modelling technique that provides spatial and temporal resolution is required, as demonstrated by various studies using mesh-based and interface-based discretization methods. The current study presents a different approach based on the orthogonal collocation method, which has been shown to be numerically efficient with high degree of accuracy.

The orthogonal collocation method discretizes the biomass particle into collocation points and solves the governing equations at each collocation point. To determine the value at an observed point, the orthogonal collocation method uses values from all discretization points, or collocation points. This leads to a significant reduction of numerical grid points compared to a mesh-based model.

The orthogonal collocation method approximates the solution of differential equations using orthogonal polynomials. There are several orthogonal polynomial trial functions that can be utilized with different orders of x and among the most common functions is shifted Legendre orthogonal polynomials, which is constructed as a function of x^2. The expanded solution for temperature at a collocation point using shifted Legendre orthogonal polynomials is described in Eq. (12), where N is the total collocation points.

$$T(x_j) = \sum_{i=1}^{N+1} d_i x_j^{2i-2} \tag{12}$$

The shifted Legendre orthogonal polynomial is defined in Eq.(13) with a =1, 2, or 3 for planar, cylindrical, or spherical geometry, respectively.

$$\int_0^1 W(x^2) P_k(x^2) P_m(x^2) x^{a-1} dx = 0 \qquad k \leq m-1 \tag{13}$$

The coordinates of the collocation points are provided by the roots of shifted Legendre polynomials, as shown in Table B.1. in **Paper I**. The first and second derivatives of Eq.(12) follow the forms that are presented in Eq.(14) and (15).

$$\frac{dT}{dx}(x_j) = \sum_{i=1}^{N+1} d_i (2i-2)\, x_j^{2i-3} \tag{14}$$

$$\frac{d^2T}{dx^2}(x_j) = \sum_{i=1}^{N+1} d_i (2i-3)(2i-2) x_j^{2i-4} \tag{15}$$

In matrix form, the expanded solution for all collocation points in Eq.(12) from the first point (i =1) to the last point (i =$N+1$) follows:

$$\begin{bmatrix} T_1 \\ T_2 \\ T_3 \\ \vdots \\ T_{N+1} \end{bmatrix} = \begin{bmatrix} 1 & x_1^2 & x_1^4 & \cdots & x_1^{2N} \\ 1 & x_2^2 & x_2^4 & \ldots & x_2^{2N} \\ 1 & x_3^2 & x_3^4 & \ldots & x_3^{2N} \\ \vdots & \vdots & \vdots & \ddots & \vdots \\ 1 & x_{N+1}^2 & x_{N+1}^4 & \ldots & x_{N+1}^{2N} \end{bmatrix} \begin{bmatrix} d_1 \\ d_2 \\ d_3 \\ \vdots \\ d_{N+1} \end{bmatrix} \tag{16}$$

$$\text{or} \quad \boldsymbol{T} = \boldsymbol{Q}\boldsymbol{d} \tag{17}$$

In order to solve the remaining unknowns in Eq.(17), which are $\boldsymbol{T}$ and $\boldsymbol{d}$, the substitution from the solution for all collocation points to the solution for each collocation point was performed with $\boldsymbol{d}$ matrix substitution.

$$\boldsymbol{d} = \boldsymbol{Q}^{-1}\boldsymbol{T} \tag{18}$$

$$T(x_j) = \left(\sum_{i=1}^{N+1} x_j^{2i-2} \right) \boldsymbol{Q}^{-1}\boldsymbol{T} \tag{19}$$

Since the remaining unknowns are equal to the total number of equations, the last form of the temperature expansion in Eq.(19) may be solved. The remaining unknowns are contributed from $N+1$ number of $T(x_j)$. The $N+1$ equations consist of the N number of

Eq.(19) at each collocation point and one additional equation originating from the surface boundary condition. The choice of trial function x_j^{2i-2} in Eq.(12), automatically ensures that the symmetry boundary condition at the center of the particle is fulfilled at each instance in time.

A similar approach may be used to the temperature's first and second derivatives, which are summarized as:

$$\frac{\boldsymbol{dT}}{\boldsymbol{dx}} = \boldsymbol{Cd} \longrightarrow C_{ji} = (2i-2)x_j^{2i-3} \longrightarrow \frac{dT}{dx}(x_j) = \left(\sum_{i=1}^{N+1} C_{ji}\right)\boldsymbol{Q}^{-1}\boldsymbol{T} \rightarrow \frac{dT}{dx}(x_j) = \boldsymbol{AT} \quad (20)$$

$$\frac{\boldsymbol{d^2T}}{\boldsymbol{dx^2}} = \boldsymbol{Dd} \rightarrow D_{ji} = (2i-3)(2i-2)x_j^{2i-4} \rightarrow \frac{d^2T}{dx^2}(x_j) = \left(\sum_{i=1}^{N+1} D_{ji}\right)\boldsymbol{Q}^{-1}T \rightarrow \frac{d^2T}{dx^2}(x_j) = \boldsymbol{BT} \quad (21)$$

At this stage, the first and second derivatives of the temperature substitution with orthogonal collocation coefficients ($\boldsymbol{A}$ and $\boldsymbol{B}$) in Eqs.(20) and (21) can be used to solve the global heat balance in Eq.(4). The orthogonal collocation methods requires that the space variable is converted into dimensionless form, with values ranging from 0 at the center to 1 at the surface, as shown below:

$$r = xR \qquad \frac{\partial T}{\partial r} = \frac{1}{R}\frac{\partial T}{\partial x} \qquad \frac{d^2T}{dr^2} = \frac{1}{R^2}\frac{d^2T}{dx^2}$$

The final form of the PDE heat balance at a collocation point in Eq.(4) is thus converted into an ordinary differential equation (ODE) system, as summarized in Eq.(22).

$$\begin{aligned}\sum \rho_{k,j} Cp_{k,j} \frac{\partial T}{\partial t} = {} & \frac{\lambda_{eff,j}}{x^a R^2}\left(ax\left(\sum_{i=1}^{N+1} A_{j,i}T_i\right) + x^a\left(\sum_{i=1}^{N+1} B_{j,i}T_i\right)\right) \\ & - \dot{r}_{v,gas,j}\, Cp_{g,j}\frac{V_p}{RA_p}\left(\sum_{i=1}^{N+1} A_{j,i}T_i\right) \\ & + \left(D_{fw,j}Cp_{fw,j}\left(\sum_{i=1}^{N+1} A_{j,i}\rho_{fw_i}\right) + D_{bw,j}Cp_{bw,j}\left(\sum_{i=1}^{N+1} A_{j,i}\rho_{bw_i}\right)\right)\sum_{i=1}^{N+1} A_{j,i}T_i \\ & - \Delta H_{dry,j}\dot{r}_{v,dry,j} - \Delta H_{dev,j}\dot{r}_{v,dev,j}\end{aligned} \quad (22)$$

Another set of equations, i.e., boundary condition and component balance, must be transformed into the orthogonal collocation format. This can be done by following the conversion of heat balance in Eq.(22) i.e., converting the dimensionless space notation and replacing the derivative term with the orthogonal collocation coefficients.

MATLAB 2016b® was used to simulate the system of coupled algebraic-differential equations, specifically the built-in ODE solver (*ode15s*). For the purpose of validating the accuracy of the orthogonal collocation method, the partial differential equations were solved directly with the built-in PDE solver (*pdepe*). A numerical accuracy test was performed by comparing the simulation results at the experimental conditions that are summarized in Table 4.

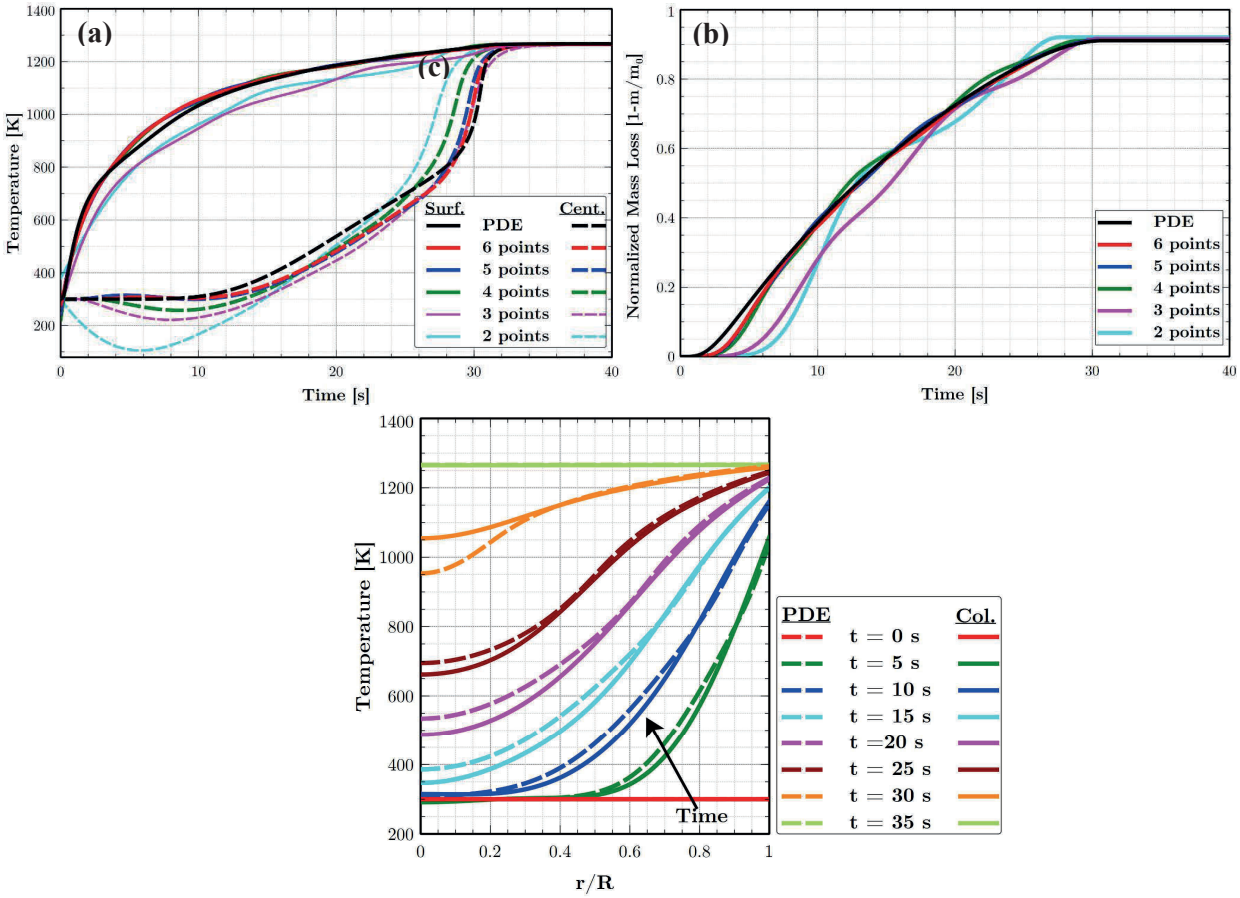

Figure 11. Grid independency test for simulation of a 9.5 mm spherical particle, (a) temperature profile, (b) normalized mass loss, and (c) temperature inside particle using six collocation points.

The results from the grid independent study are summarized in Figure 11. According to the analysis, using six collocation points achieved the highest degree of agreement with almost the same accuracy as the PDE solver, which uses 200 computational grids. The utilization of more than four collocation points was found to produce insignificant improvement in the simulation results. However, six collocation points were used for the rest of the analysis, which gives a margin for reaction kinetic schemes with higher activation energies which cause narrower reaction zones inside the particle. The computational efficiency was maintained since the computational time did not increase drastically by utilization of six collocation points.

4.1.3. Moving coordinates

Temperature profile based on the heat balance in Eq.(4) must be corrected as a result of the orthogonal collocation method's conversion of the spatial variable into dimensionless form. The accumulation term must be revised during particle shrinkage since the space variable is confined between 0 and 1, even while the physical dimension, i.e., particle radius, varies over time due to char reaction $\left(R = f(t)\right)$. The corrected temperature is given by Eq.(23)

$$T_{new} = T_{old} + \frac{1}{R}\frac{\partial T}{\partial x}\frac{\partial R}{\partial t}dt \tag{23}$$

In the first derivative form, Eq.(23) gives:

$$\frac{\partial T_{new}}{\partial t} = \frac{\partial T_{old}}{\partial t} + \frac{1}{R}\frac{dT}{dx}\frac{dR}{dt} \tag{24}$$

Eq.(24) can be replaced with the accumulating term in Eq.(4) to produce a modification of the accumulation term, as presented in Eq.(25). Eq.(25) is discretized using orthogonal collocation, as presented in Eq. (26).

$$\sum \rho_k Cp_k \left(\frac{\partial T}{\partial t} + \frac{1}{R}\frac{\partial T}{\partial x}\frac{\partial R}{\partial t}\right) \tag{25}$$

$$\sum \rho_k Cp_k \left(\frac{\partial T}{\partial t} + \frac{1}{R}\left(\sum_{j=1}^{N} A_{i,j} T_j\right)\frac{\partial R}{\partial t}\right) \tag{26}$$

The relevance of incorporating the moving coordinate term in modelling a shrinking particle is presented in Figure 12 for simulation of a 9.5 mm diameter spherical particle. The difference is not significant considering the minor effect it has on the evolution of the predicted particle mass and radius. In Eq. (25), the $\partial T/\partial x$ term cancelled $\partial R/\partial t$, this resulted in a minor difference in temperature and mass evolution. As a result, this effect was neglected in the current study.

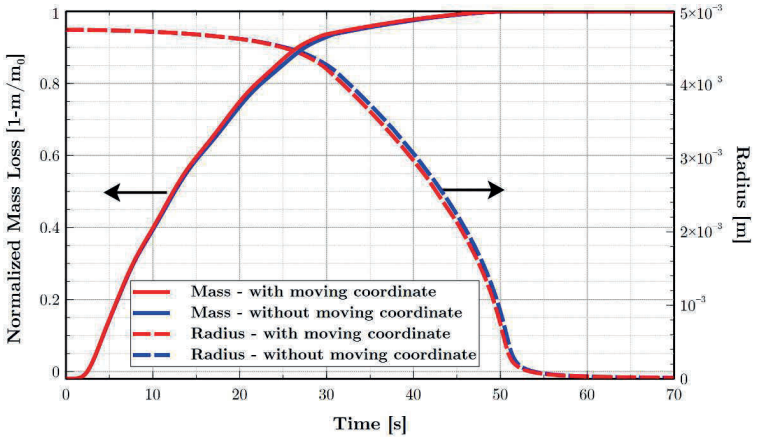

Figure 12. Comparison of normalized mass loss and radius for simulations with and without moving coordinate term for combustion of a 9.5 mm spherical particle.

4.1.4. Source term evaluation

Inside a biomass particle, the decomposition is a continuous process that progresses from the particle surface to the particle center at a rate defined by the propagation of the heat wave. The reaction rate is determined only at certain collocation points using the orthogonal collocation approach. Because the temperature was insufficient to start the reaction at the inner collocation points while the reaction was finished at the outer collocation point, the use of a kinetic rate with very high activation energy or a small reaction zone resulted in an unsmooth transition. This may result in a fluctuation of the mass loss and an uneven release of pyrolytic gases and water vapor, which might cause challenges to obtain convergence in CFD simulations.

The use of more collocation points is expected to alleviate this problem. However, this will increase the computational cost. An alternative solution used in the current work is to expand the coverage of the reaction rate at one specific collocation point. The idea behind the

improvement is to evaluate the reaction rate in the area between each collocation point and bring the average reaction rate over the area into the collocation point. The mass weighted average was used to calculate the average reaction rate which follows Eq.(27), where k= reaction and components index, i = collocation points index, j = Euclidean points index and l = expansion points index.

$$\bar{\dot{r}}_{v,k,i} = \frac{\int_{r_{j-1}}^{r_{j+1}} A_{k,l} \exp\left(-\frac{E_{a_k}}{R_g T_l}\right) \times \rho_{k,l} \times A_{layer,l}\, dr}{\int_{r_{j-1}}^{r_{j+1}} \rho_{k,l} \times A_{layer,l}\, dr} \times \rho_i \tag{27}$$

$(j+1)$ and $(j-1)$ are the Euclidean points to a collocation point's left and right side. The Euclidean point was calculated based on the middle position of adjacent collocation points. $A_{layer,j}$ is the area perpendicular to the expansion layer, which is, $4\pi r^2$ for spherical, $2\pi r L_p$ p for cylindrical, and $L_p \times W_p$ for planar geometry. The reaction rate was evaluated for expansion points that were located between two Euclidean points, and the mass weighted average reaction rate was used as the reaction rate source term at each collocation point.

Based on the interpolated temperature and density values, the reaction rate at the Euclidean points and any other expansion points outside the collocation points were determined. Different interpolation methods were employed herein for density and temperature as discussed below. The solution of the expansion form of temperature may be used to compute temperature in Eq.(12), as long as the value of d is available. The value of d is calculated using Eq.(18) since the value of Q, which is a function of x, and T are available.

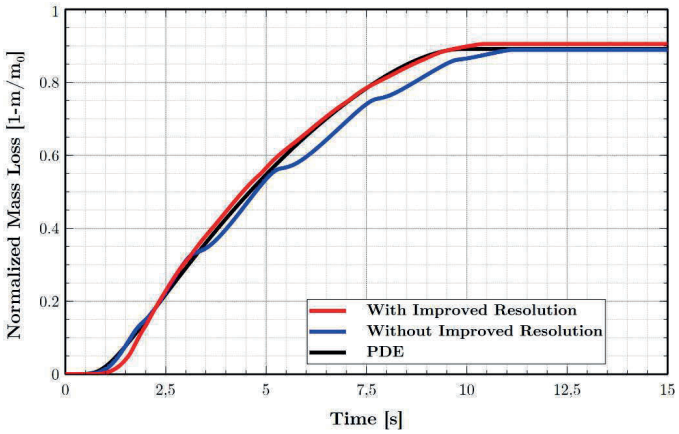

Figure 13. Normalized mass loss results with and without improved resolution of reaction rate (using Eq.(27) for a 5 mm spherical particle).

The density at the expansion points were interpolated using the piecewise cubic hermite polynomial method, which has been proven to produce better results than quadratic and linear interpolations in assessing the reaction rate correction in the sub-grid scale models [95]. The piecewise cubic hermite polynomial method using a third-order polynomial to calculate the dependent variable at the observed point is shown in Eq. (28). The coefficients of the cubic interpolation are derived from the value from adjacent points [96].

$$\rho_k(x) = a(x - x_{i-1})^3 + b(x - x_{i-1})^2 + c(x - x_{i-1}) + d \tag{28}$$

Figure 13 highlights the importance of using improved resolution of the reaction rate source term particularly when the devolatilization reaches the inner collocation points where the distance between the points is wider.

4.1.5. Stefan flow effect

The nominal Nusselt and Sherwood number formulation, as summarized in Table 4 of **Paper I**, has to be modified by accounting for the gaseous flux out from particle, i.e., Stefan flow. The corrected Sherwood and Nusselt number formulation from Michaelides [97] was utilized and compared with the simulation without any correction due to Stefan flow as summarized in Figure 14. It is assumed the material is isotropic allowing an even flow of gas through the boundary layer, while in reality the flow can be larger in the fiber direction and also effected by intermittent bursts due to cracks in the material.

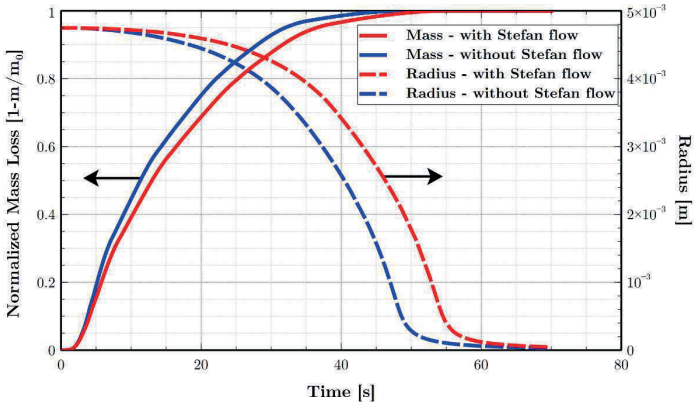

Figure 14. Comparison of simulations results with and without accounting for the Stefan flow effect for combustion of 9.5 mm spherical particle.

The Stefan flow effect began to make a significant contribution when the particle surface reached the char reaction temperature (about 800 K) at t>5 s since the Stefan flow limited the oxidative gas from penetrating the particle surface boundary layer. Since the exothermic char reaction has almost as strong influence as the contribution from radiation heat, the reduction in the char reaction rate had a major impact on the total heat and mass balance. Based on this assessment, it can be concluded that accounting for the Stefan flow in particle combustion cannot be neglected.

4.2. Single particle pyrolysis and combustion modelling using orthogonal collocation

4.2.1. Pyrolysis experiment

A comparison of the present simulations with pyrolysis experiments is shown in Figure 15a-d. Particle surface temperature, particle center temperature, and mass evolution during conversion were selected as the criteria to evaluate the agreement between simulated and experimental findings.

Figure 15a shows that the predicted mass loss was quite close to the experimental data for different particle characteristics. The dry spherical particle displayed faster mass reduction than the dry cylinder and wet cylinder particles. Furthermore, both dry particles leveled out at lower mass loss than the moist particle, as predicted.

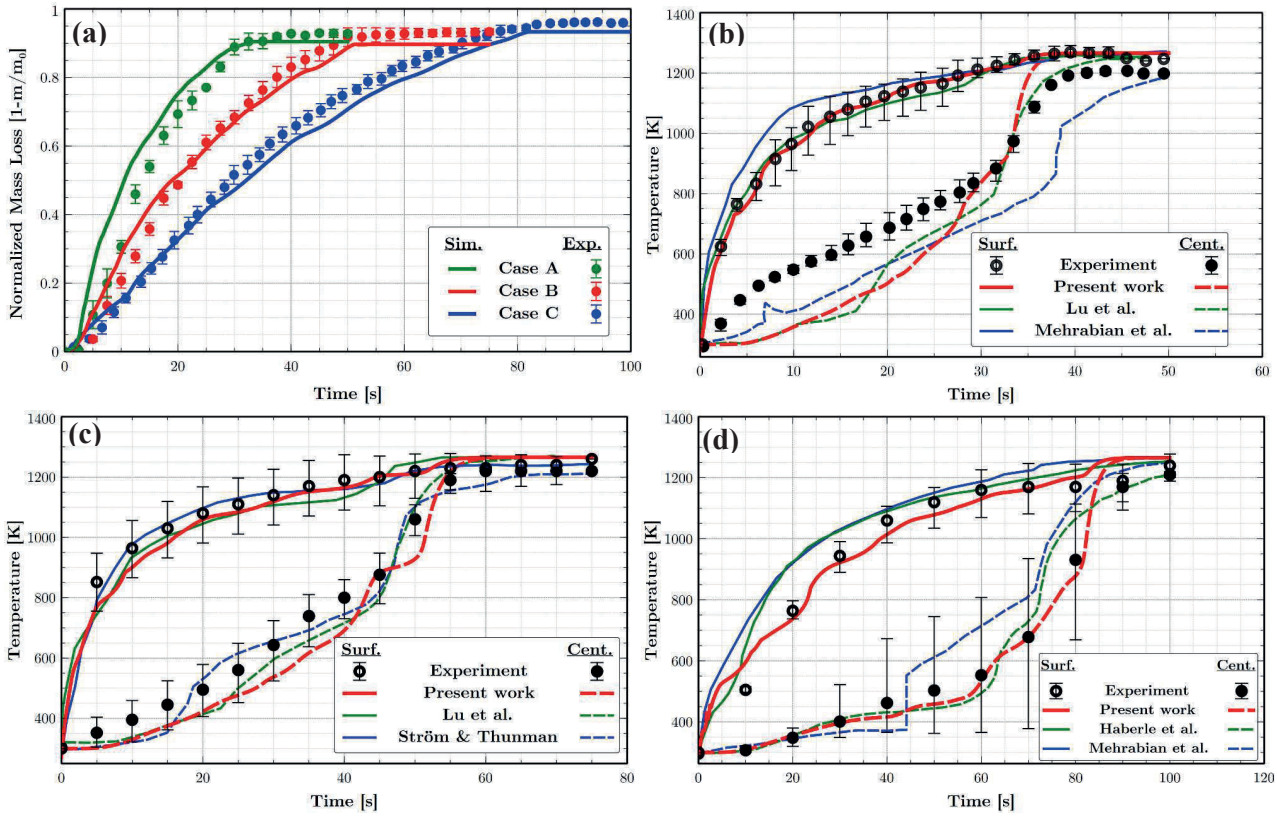

Figure 15. Comparison between simulated and measured (a) normalized mass loss for Case A, B, and C, (b) temperature for Case A, (c) temperature for Case B, and (d) temperature for Case C.

The only significant difference in temperature prediction was related to the prediction of the center temperature, as shown in Figure 15b. The literature [36] has addressed the difficulty of measuring the center temperature of a spherical particle. Unreliable measurement is thought to be the result of lateral heat conduction from the thermocouple's outer parts, which leads to a rapid increase in the center temperature.

The mesh-based model is the most sophisticated model and is expected to produce more accurate results because it uses higher resolution than the orthogonal collocation-based model and the interface-based model. However, the comparison shown in Figure 15b-d suggests that the orthogonal collocation approach can maintain simulation accuracy. The comparison with previous simulations leads to the conclusion that the current simulation produced almost similar accuracy as with the mesh-based and the interface-based models. These results are promising considering that the present study does not rely on tuning physical parameters and that the surface boundary condition is determined directly from the balance equation of heat transport at the particle surface. In some published studies, physical model parameters have been tuned e.g., heat of devolatilization and shrinkage factor, and occasionally experimentally determined surface temperature has been used as boundary condition to improve the simulation result. Notably, the experimental uncertainties for temperature readings were rather substantial, as seen by the large error bars, making it difficult to determine which of the models agrees best.

4.2.2. Combustion experiment

The particle combustion simulation results are shown in Figure 16a and b, and includes surface temperature, center temperature, and normalized mass loss as a function of time. The prediction of the normalized mass loss nearly overlapped with the experimental data.

However, there were significant differences in the prediction of center and surface temperatures, as shown in Figure 16a. The disparity in center temperature, as previously explained in the preceding section, is caused mostly by the inaccuracy of the thermocouple measurement. Because the particle began to decrease while the thermocouple bead stayed in its constant place, the surface thermocouple did not measure the right temperature. When the particle began to shrink, the surface thermocouple began to monitor the gases around the particle rather than its surface.

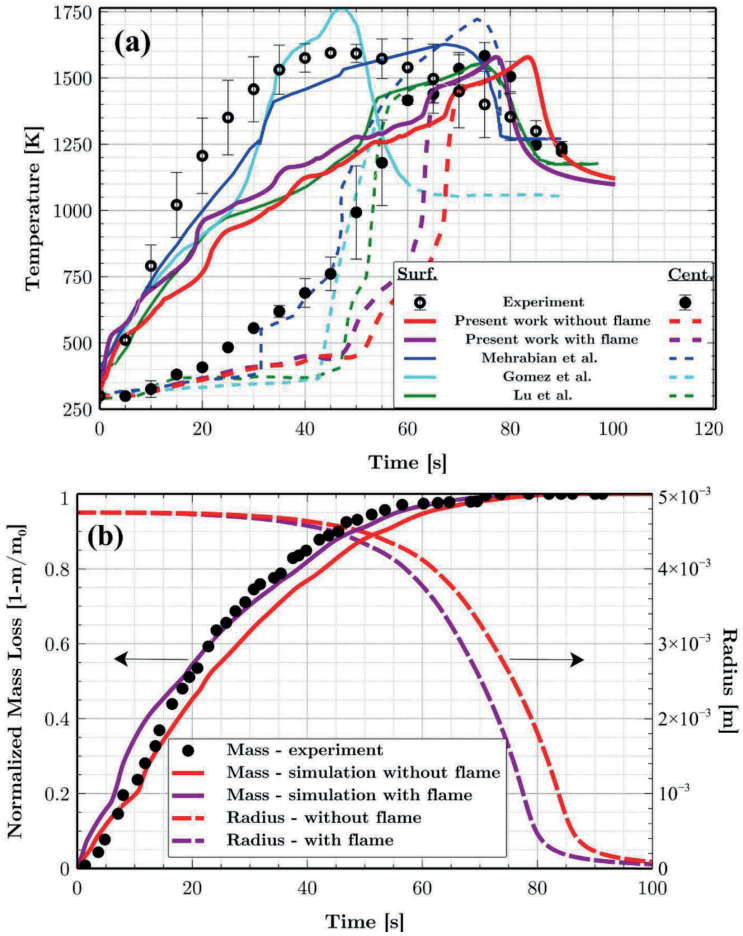

Figure 16. Comparison between simulation results and experimental data for Case D, (a) particle surface and center temperatures (b) normalized mass loss.

When compared to prior simulations, the mesh-based simulation from Lu et al, which neglect the existence of flame in the gas phase, provided comparable results to the collocation-based simulation, which also excludes the presence of flame in the gas phase (red line in Figure 16). Meanwhile, Mehrabian et al. and Gomez et al. interface-based model, which includes flame due to combustion in the gas phase using CFD simulation, produced a significant offset compared to the other two simulation methods but gave a prediction closer to the experimental

temperature. Mass evolution is more reliable to use for model validation considering the significantly lower error bars for mass evolution than for temperature measurements.

A sensitivity analysis of the shrinkage factors due to drying and devolatilization was performed and summarized in Figure 17. The shrinkage factors due to drying and devolatilization are accounted for in the model by the parameters β_m and β_b in Eq. (11). Various shrinkage factor values were chosen based on values provided in the literature i.e., 20% [36], 25% [39], and 50% [32]. The recommended values were only used as shrinkage parameters due to devolatilization in this current investigation. The investigation demonstrates that the larger the value of the shrinkage factor, the faster the particle conversion. As shown in Figure 17, 20% shrinkage factor gave better result compared to the nominal case without particle shrinkage.

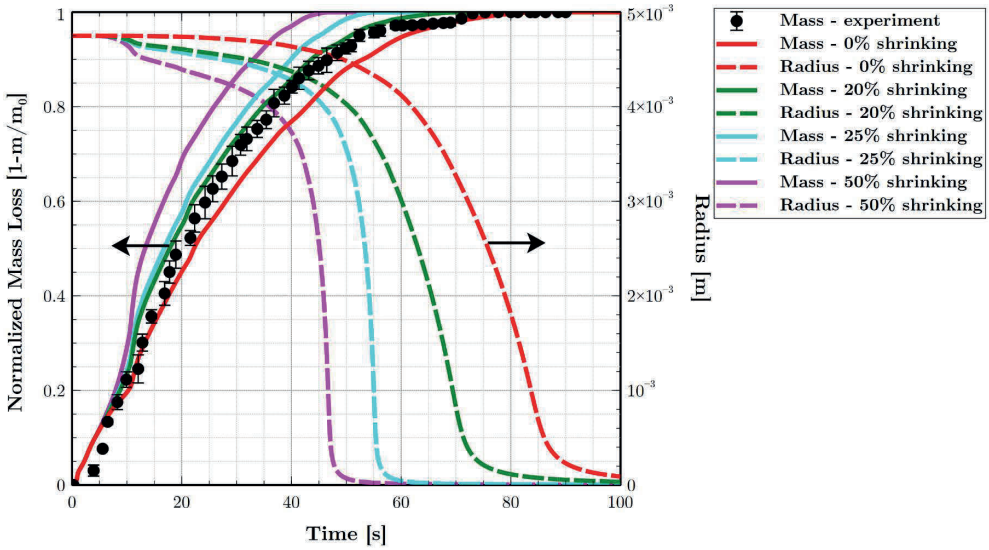

Figure 17. Sensitivity analysis of particle shrinkage.

Even better prediction of particle mass and temperature is obtained by inclusion of radiation from flame due to combustion in the gas phase as depicted in Figure 16 with purple line. The radiative heat source was included in the heat balance at the boundary condition in Eq. (4) by assuming that the flame temperature was 2000 K and the gas emissivity was about 0.2. A dynamic coupling of solid and gas phase is required to predict accurately fluctuating and uninformed radiative feedback to the solid which will affect the conversion of the biomass particle [98].

4.2.3. Model efficiency

The simulation time was recorded and compared to previous works to quantify the cost of implementing the new particle model, since efficiency is a crucial factor to consider when determining whether the particle model can be implemented as a sub-grid function in CFD analysis. The simulation time in the present study depended on the number of collocation points and was in the order of seconds, but the time can be further reduced by code optimization and compilation.

A previous study using the mesh-based discretization method recorded that at least 2930 seconds (48 minutes) were required to simulate experimental Case B [19]. The findings show

that the simulations are three orders of magnitude faster while keeping the same accuracy as the mesh-based model. The short simulation time needed in the present study was considered promising in that a single particle can be implemented in a CFD analysis to describe a bed of particles, which allows full coupling with local gas flow and the temperature surrounding the particles.

4.3. Mass transfer to and from a particle with Stefan flow effect

4.3.1. Model formulation

In particle combustion and pyrolysis, there is a convective outflow from the particle due to drying and devolatilization that influence the diffusional transport and the penetration of convective flow from the surrounding gas to the particle surface. Therefore, instead of only considering the flow from the surrounding gas, the net flow between Stefan flow and the surrounding gas flow should be utilized to predict a more correct heat and mass exchange from or to the particle surface.

Using a total mass flux at the surface, an analytical method for predicting mass transfer to and from a particle with the Stefan flow effect was derived. The dimensionless number, $An = \frac{u_s R}{D}$, is used to calculate the final form of mass transfer in the particle film layer. Assuming that there is no change in film thickness due to Stefan flow, the final form of the analytical solution for the corrected Sherwood number can be expressed as Eq.(29). The detailed derivation has been presented in **Paper II**.

$$Sh_{eff} = \frac{2.An}{e^{\frac{2An}{Sh}} - 1} \tag{29}$$

The degree of accuracy and range of applicability of the analytical solution was evaluated further by a comparison with CFD simulations and compared with classical Sherwood number corrections due to Stefan flow.

4.3.2. CFD simulation of Stefan flow effect

The current analytical solution for an effective Sherwood number due to the effect of Stefan flow was validated by comparing the results from the analytical solution with CFD simulation using ANSYS Fluent. The CFD simulations presented here are constrained to laminar flow, i.e., bulk Reynolds numbers < 800 and low particle Reynolds numbers, Re_p, where mass and heat transfer are steady. For the current spherical particle study, the particle Reynolds number was kept below 150 to maintain a steady Sherwood number and avoid periodic vortex shredding.

A particle was modelled as a thin hollow sphere with the thickness $0.01\ d_p$. A very fast irreversible reaction of $A \rightarrow A^*$ at the particle surface was used, which produced zero concentration of A everywhere except on the particle surface. The stoichiometry of $A \rightarrow A^*$ eliminates a net flow due to the reaction. The source of Stefan flow was a mass source in the thin particle surface which produced the same flow rate in all directions. This setup corresponds to a particle with equal heating rate on the whole surface e.g., by uniform radiation or very high heat conductivity. Simulations were done for a range of Stefan flow.

The computational domain was cubic with a length 20 times larger than the particle radius to avoid any significant velocity increase around the particle. A high-quality mesh of prism layers in the surface region were used as depicted in Figure 18 to minimize numerical diffusion. Mesh independent result was achieved for 3.3 million cells after an adaption that used the gradient of species and pressure.

The boundary conditions used in the simulation were: the inlet flow was set as velocity boundary condition, the outlet condition was set as outflow, a free slip condition at the walls, and no-slip condition at the particle surface. The continuity, momentum and species balance were calculated using Eqs.(30), (31)and (32) in ANSYS Fluent 19.0 [99].

$$\frac{\partial \rho}{\partial t} + \nabla \cdot (\rho \vec{v}) = S_m \tag{30}$$

$$\frac{\partial}{\partial t}(\rho \vec{v}) + \nabla \cdot (\rho \vec{v}\vec{v}) = -\nabla p + \nabla \cdot (\bar{\bar{\tau}}) + \rho \vec{g} + \vec{F} \tag{31}$$

$$\frac{\partial}{\partial t}(\rho Y_i) + \nabla \cdot (\rho \vec{v} Y_i) = -\nabla \cdot \vec{J_\iota} + R_i + S_i \tag{32}$$

The pressure-velocity coupling was handled using the SIMPLE algorithm, and the equations were discretized using second-order accurate schemes. The governing equations were solved using a segregated solver approach.

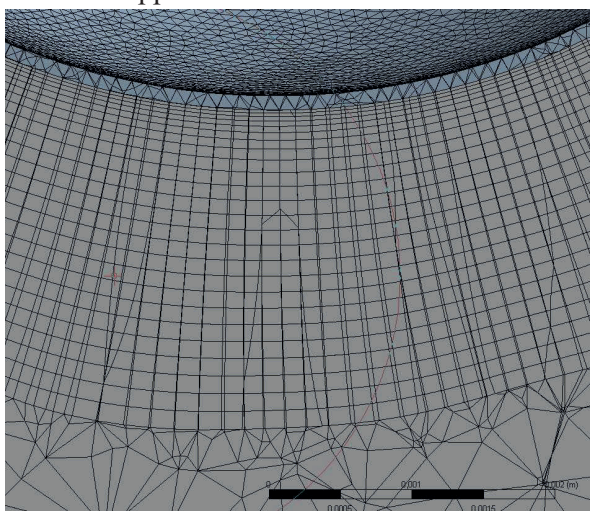

Figure 18. Cross section in the computational mesh.

The formation of A^* was limited by the transport of A to the surface. As a result, the Sherwood numbers for transport with Stefan flow may be approximated using the net outflow of A, as presented in Eq.(33), or from the outflow of A^*, as presented in Eq.(34). The third way of determining the Sh number was using the volume integral of the reaction rate in the porous volume, as given by Eq.(35). To verify the simulation accuracy, the Sherwood number evaluations from those three distinct approaches were compared.

$$Sh_{CFD} = \frac{d_p}{D_A \Delta C_A \, A_p} \left(\int_{A_{inlet}} u_x C_A dA_{inlet} - \int_{A_{outlet}} u_x C_A dA_{outlet} \right) \tag{33}$$

$$Sh_{CFD} = \frac{d_p}{D_{A^*}\Delta C_{A^*}}\left(\frac{\int_{A_{outlet}} u_x C_{A^*} dA_{outlet}}{A_p} - u_s C_{A_s^*}\right) \quad (34)$$

$$Sh_{CFD} = \frac{d_p}{D_A \Delta C_A \, A_p} \int_{V_{porous}} r_A dV \quad (35)$$

4.4. Sherwood number correction with and without Stefan flow

4.4.1. Sherwood number correction without Stefan flow

A new model was developed and fitted with the results of the CFD simulations. The new Sherwood number without Stefan flow follows Eq.(36).

$$Sh = 2 + 0.486\, Re^{0.534} Sc^{0.408} \quad (36)$$

This new model gave a significantly better fit compared to CFD simulation data as seen in Figure 19 compared the old Sherwood number formulation e.g., Ranz-Marshall [100], Clift [101], and Frössling [102], particularly at high Sc number.

$$Sh = 2 + 0.522\, Re^{1/2} Sc^{1/3} \qquad \mathrm{Re} < 150\,;\, 0.5 < \mathrm{Sc} < 2 \quad (37)$$

$$Sh = 2 + 0.6\, Re^{1/2} Sc^{1/3} \qquad Re < 150\,;\, 0.5 < Sc < 2 \quad (38)$$

$$Sh = 1 + (1 + \ Re\ Sc)^{1/3} f(Re) \qquad Re < 400\,;\, 0.24 < Sc < 100 \quad (39)$$

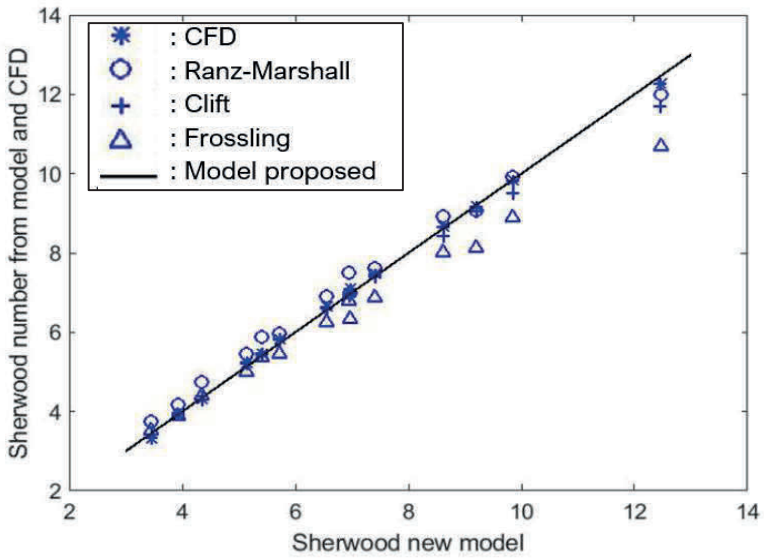

Figure 19. Comparison between the new model (the solid line), CFD simulation and old Sherwood number correlations in different range of Sc numbers (0.5<Sc<3).

4.4.2. Sherwood number correction with Stefan flow

In this sub-section, the validation of the analytical solution of Sherwood number correction due to Stefan flow is compared with the CFD simulation results. The simulations and calculations were conducted not only for system with even and uneven Stefan flow but also for different Schmidt, Andersson, and Reynolds numbers. Two classical Sherwood number

corrections due to Stefan flow are also presented, i.e., the Spalding [103] and Abramzon et.al. [104] correlations.

The best agreement between simulation results of even Stefan flow and calculation from the new model is obtained with Eq.(40). The calculated Sh_0 from Eq.(40) is used to calculate the effective Sherwood number in Eq.(29). The formulated model in Eq.(40) contains the dependence on An/Sc which allows to reduce the model residual to less than 3% and reduce residual dependence due to different Schmidt number. A comparison between the new model and the traditional models from Spalding [103] and Abramzon et.al. [104] is provided in Table *5* which demonstrate the new model's capacity to predict the Sherwood number better than previous models.

$$Sh_0 = 2 + 0.486\, Re^{0.534} Sc^{0.408} - 0.0576\, An^{0.49}/Sc^{1.41} \tag{40}$$

Table 5. Summary of models for Sherwood number with even Stefan flow

Model	Formulation	Relative error range
Proposed model	$Sh_{eff} = \frac{2.An}{e^{\frac{2An}{Sh_0}}-1}$ with $Sh_0 = 2 + 0.486\, Re^{0.534} Sc^{0.408} - 0.0576\, An^{0.49}/Sc^{1.41}$	-0.02 to +0.03
Spalding [103]	$Sh_{eff} = \frac{\ln(1-B_M)}{B_M} Sh_0$ with $B_M = \frac{Y_{vs}-Y_{v\infty}}{1-Y_{vs}}$	-0.12 to +0.03
Abramzon et.al. [104]	$Sh_{eff} = \frac{\ln(1+B_M)}{B_M} Sh^*$ with $Sh^* = 2 + \frac{Sh_0-2}{F_M}$ and $F_M = (1+B_M)^{0.7} + \frac{\ln(1+B_M)}{B_M}$	-0.2 to +0.1

The majority of empirical data on evaporation and empirical models are created for convective heating systems, which induce an uneven Stefan flow in the boundary layer. According to the present CFD analysis, approximately 72% of the mass transfer to a particle occurs in the upstream half of the particle surface. The current study also discovered a marginal difference in film thickness between the even and uneven Stefan flow as depicted in Figure 20.

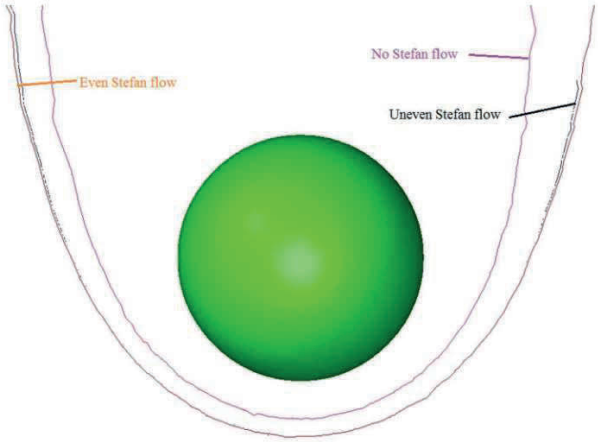

Figure 20. Contours of concentration of $C_A = 0.95C_{A,bulk}$ with and without Stefan flow.

Slight modification of Sh_0 from Eq.(40) for even Stefan flow is needed to obtain good prediction of mass transfer to particles experiencing uneven Stefan flow as prescribed in Eq.(41). The calculated Sh_0 from Eq.(41) is used to calculate the effective Sherwood number in Eq.(29). This proposed model gives residual error less than ±4% compared to the CFD simulation results. The current model is proven to be more accurate in predicting mass transfer in systems with uneven Stefan flow compared to the traditional models, e.g., Spalding [103] and Abramzon et.al. [104] correlations, as reported in **Paper II**.

$$Sh_0 = 2 + 0.486\ Re^{0.534}\ Sc^{0.408} - 0.118\ An/Sc^{0.25} \tag{41}$$

A comparison between the proposed model and the traditional models is provided in Figure 21. Existing models have mainly been developed for water evaporation and produce quite accurate prediction for water evaporation with Schmidt number close to 0.66 at 300 K.

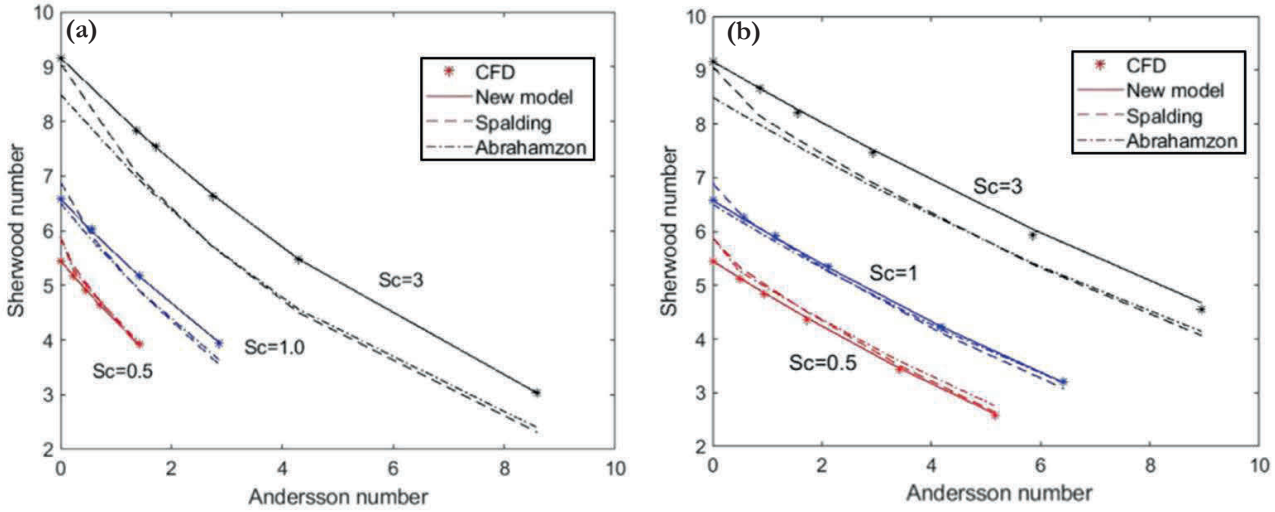

Figure 21. Comparison between models with (a) even Stefan flow and (b) uneven Stefan flow at Re = 66 and different Sc numbers.

5. CFD Analysis of Biomass Combustion in The Grate Fired Furnace

This chapter expands on the CFD simulation research to predict the behavior of biomass combustion in the experimental facility that was presented in Section 3. In the current investigation, two simulation approaches were used: steady and transient simulations. The global behavior of biomass combustion at various combustion conditions was predicted using steady simulation. To verify simulation accuracy, average values of several key combustion parameters, such as temperature and CO_2 concentration, were compared to experimental results. The flow field characteristics inside the furnace were further used to provide a better understanding of the PM emissions obtained in the experiments. Eventually, the discrete particle model (DPM) was utilized to predict the kinetics of PM reduction throughout the furnace.

Furthermore, transient simulations were carried out to obtain a better understanding of the biomass combustion characteristics over a biomass reloading cycle. In this simulation study, the use of a more detailed devolatilization scheme was investigated by including lignocellulosic components and estimating pyrolysis products. To ensure modelling accuracy, the dynamic profiles of CO_2 and temperature over one biomass reloading cycle was compared to the time-resolved experimental values. The influence of different lignocellulosic components on PM emissions was then assessed qualitatively and quantitatively. Local flow field condition from CFD analysis over one biomass reloading cycle can provide a better understanding of PM formation and reduction mechanisms during biomass combustion e.g., local and instantaneous PM precursors concentration, oxygen concentration, and temperature level.

5.1. Steady CFD simulation

5.1.1. Global mass balance analysis

Based on the reaction scheme (R.1–R.3) and the ultimate and proximate analyses in Table 1, a global mass balance calculation was formulated. These reactions include thermal decomposition of biomass, vaporization of bound water (7.6%), formation of volatile matter (72.4%), and solid char (19.4%) in reaction R.1. Volatile gas is burned in reaction R.2, and char is burned in reaction R.3. The ultimate analysis of the biomass, which is presented in Table 1, was used to determine the chemical composition of the biomass. The analysis of the mass balance provides data about the air leakage into and out of the furnace.

$$CH_{1.57}O_{0.717} \rightarrow 0.597\, CH_{2.27}O_{1.013} + 0.410\, C + 0.107\, H_2O \quad \text{(R.1)}$$

$$CH_{2.27}O_{1.013} + 1.063\, O_2 \rightarrow CO_2 + 1.139\, H_2O \quad \text{(R.2)}$$

$$C + O_2 \rightarrow CO_2 \quad \text{(R.3)}$$

5.1.2. Simulation setup

The details of the steady simulation setup have been provided in **Paper III**. In the current work, ANSYS 2020 R1 was used to create the 2-dimensional furnace geometry and the computational mesh. ANSYS Fluent was used to do the CFD simulation. The final mesh, as depicted in Figure 22, has passed the mesh independence test and delivered an average wall y^+ value of roughly 2.5 at the furnace freeboard. Temperature probe locations are in accordance with the experimental study and displayed in Figure 22.

Steady state 2D CFD simulation was conducted by using transition SST model in combination with the eddy dissipation concept for the volumetric volatile gas reaction (R.2). Biomass, char and grate were defined as porous bodies. Heat of combustion was accounted for by the exothermic heat of reaction from volatiles burning and char heat of reaction. Char combustion was defined using source term for CO_2 and energy and sink term for O_2. Primary air flow is injected from the bottom part of furnace with turbulence length scale and intensity condition calculated based on real experiment condition. The wall boundary condition was also defined based on the condition in experimental facility i.e., 5 mm of steel wall and 20 cm insulation.

The Discrete Particle Model (DPM), i.e., Lagrangian time resolved particle tracking, including the particle radiation and convection heat transfer models along with the Discrete Random Walk (DRW) model is utilized to simulate the particulate matter. Inert particles with a diameter of one micrometer were injected into the system from a surface 10 cm above the biomass layer. The particle injection surface is positioned in the flame area, which is where PMs are frequently formed. This allows particle time history analysis (residence time and temperature) to the outlet.

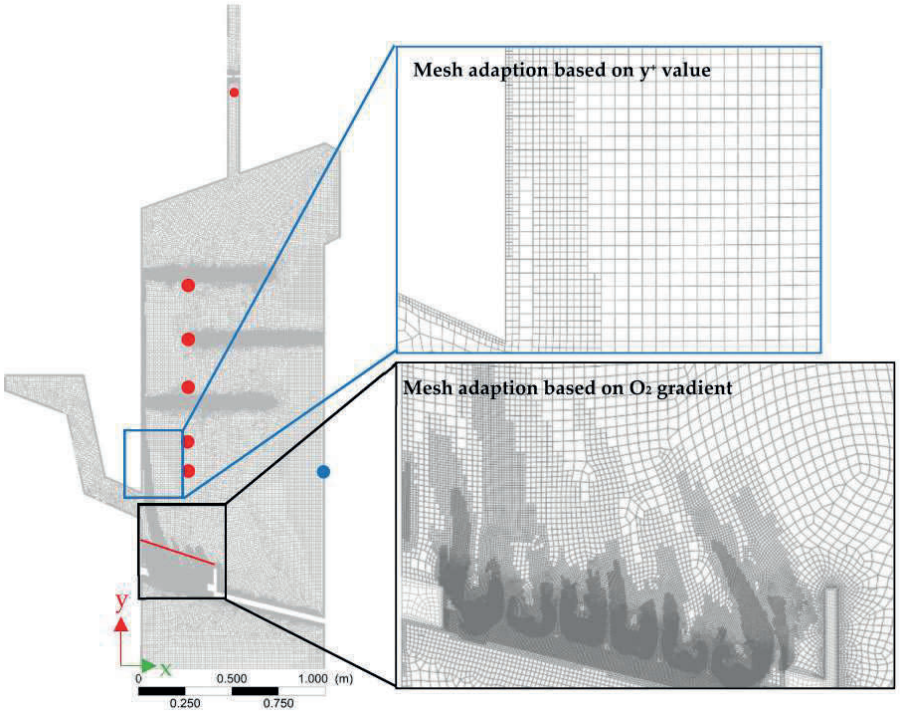

Figure 22. Simulation model for CFD analysis (● : temperature probes located at 100, 115, 145, 175, 205, and 305 cm from ash pit; ● : wall temperature probe at 100 cm from ash pit)

5.1.3. PM reduction kinetics

The kinetic analysis of PM reduction in the furnace is based on DPM simulation results (particle time, temperature, and coordinates) and experimental PM observations. To ensure the stability and accuracy of the kinetic study, 3000 particles were injected. The governing equation used in the kinetic investigation is shown in Eqs.(42) and (43). The remaining mass of PM, the local oxygen concentration, and the particle temperature, influence the rate of PM reduction. Non-linear regression was used to calculate the pre-exponential factor $\left(k\left(T_{ref}\right)\right)$ which is the rate constant at the reference temperature, and the activation energy (E_a) in the centered Arrhenius kinetic form.

$$\frac{dC_{PM}}{dt} = k(T)\, C_{PM}\, y_{O_2} \tag{42}$$

$$k(T) = k\left(T_{ref}\right) \exp\left[-\frac{E_a}{R}\left(\frac{1}{T + 273.15} - \frac{1}{T_{ref} + 273.15}\right)\right] \tag{43}$$

5.1.4. Global prediction of biomass combustion

A CFD simulation of biomass combustion is conducted to quantify parameters that are difficult to acquire experimentally. Thermocouples, for example, cannot survive high temperatures in the flame zone, whereas CFD can predict the temperature distribution over the whole furnace. CFD also provides information on the flow field inside the furnace, as well as particle temperature and particle residence time distribution.

The CFD simulations were validated by comparing simulation results to experimental data. In general, the measured and simulated exhaust gas temperatures and CO_2 concentrations correspond well for all observation locations, as summarized in Table 6. The CFD model also predict the right temperature trends for variations in air/fuel ratio, air pre-heating, and furnace baffle installation. This assures that further analysis can be performed using the simulation results to estimate the PM reduction kinetics.

Table 6. Temperature and CO_2 composition from measurement and simulations.

Experiment ID	% mole CO_2			Thermocouples average (°C)			Chimney (°C)			Wall (°C)		
	Exp		CFD	Exp		CFD	Exp		CFD	Exp		CFD
Exp 1	9.59	±0.35	10.2	772	±7	771	819	±9	813	733	±5	732
Exp 2	9.95	±0.77	10.2	828	±11	800	854	±31	833	761	±7	763
Exp 3	10.5	±0.4	10.6	795	±8	796	846	±12	828	789	±3	759
Exp 4	10.1	±0.78	10.2	810	±25	847	770	±7	759	764	±5	797
Exp 5	9.78	±0.43	10.2	833	±24	871	801	±4	783	764	±4	823

*Chimney temperature sampled at 305 cm from ash pit; thermocouples average is the average value of 100, 115, 145, 175 and 205 cm thermocouple measurement. Experiments errors are reported as standard deviation from measured data. See Figure 22 for detail thermocouple coordinate.

5.1.5. Influence of different operating condition to PM emission

Different operating conditions was arranged in the current work to understand its influence to PM emission in the biomass combustion system. Different gas residence time was

prepared using baffles installation, while different temperature and stoichiometric condition were prepared using air pre-heating and different air/fuel ratio. The PM concentration experimental results, as summarized in Figure 23, are consistent with current knowledge of PM emissions under various combustion conditions. Different operating parameters, such as residence time, combustion temperature, and air/fuel ratio, have a significant impact on emissions levels. Increases in residence time, primary air temperature, and air/fuel ratio, decrease PM emissions by up to 80% within the range of experimental conditions investigated.

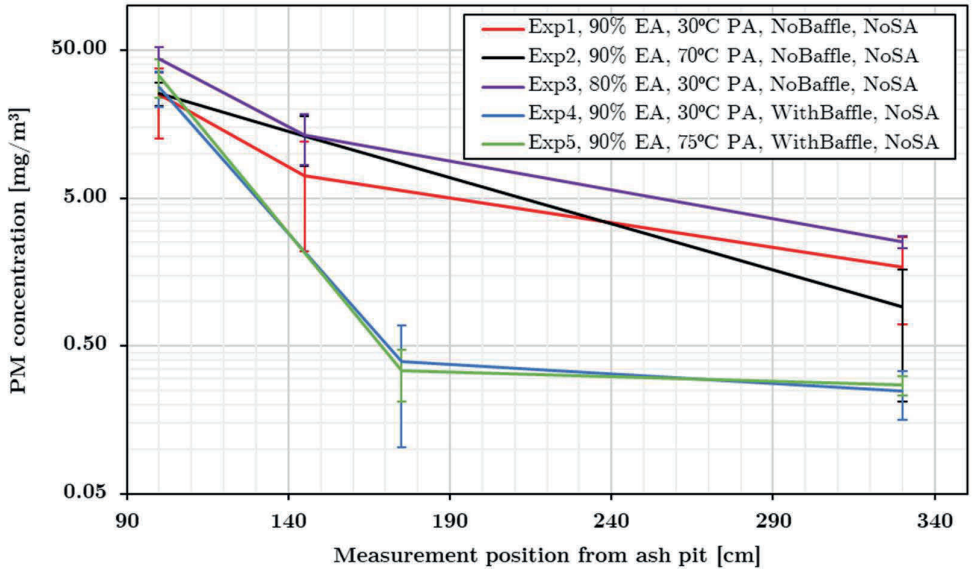

Figure 23. PM_{10} measurement result for the system with and without baffle and for the system, with and without primary air preheater, and different levels of excess air. (EA: excess air, PA: primary air, SA: secondary air)

5.1.6. Kinetics study of PM

The kinetic analysis of PM reduction is conducted based on a model for soot combustion. CFD simulation results indicate that the oxygen mole fraction along the particle trajectories is relatively constant i.e., around 0.09. By injecting 3000 particles on the injection line, results are found to be number independent.

Non-linear regression analysis was used to analyze the kinetic parameters for PM reduction. The reaction kinetic model parameters for PM reduction are obtained to 23.1 (s^{-1}) for the rate constant at reference temperature (900°C) and 126.2 (kJ mol^{-1}) for the activation energy. The correlation coefficient for the overall model is determined to be 99.0%, confirming that the model achieves its goal of predicting PM reduction throughout the furnace. A comparison between calculated and experimentally measured PM concentrations is provided in Figure 24. The observed activation energy is consistent with the range of activation energies for soot oxidation reported in previous research i.e., 102 to 210 (kJ mol^{-1}) [105].

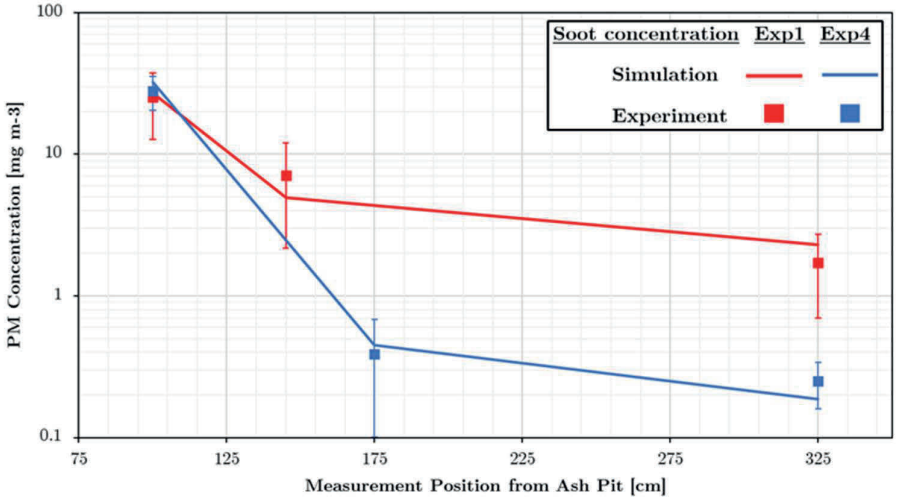

Figure 24. Comparison of experimental and calculated PM concentrations.

5.2. Transient CFD simulation

Time-resolved CFD simulation is performed as an improvement to the steady state CFD simulation analysis, allowing for a more precise prediction of instantaneous and local combustion conditions. The enhancements include the use of lignocellulosic components (cellulose, hemicellulose, and lignin), the prediction of devolatilization products, the use of a two-step Tesner model for soot formation and reduction and convolution of CFD simulation results to account for the dispersion in the sampling system.

5.2.1. Prediction of devolatilization product

The biomass devolatilization scheme used in the current work is similar to that proposed by Miller and Bellan [40] as depicted in Figure 1d. The decomposition of each lignocellulosic compound to the active component can be calculated using Eqs. (44) to (48) and the kinetics parameter are summarized in Table 7.

Table 7. Kinetic parameters in the Miller and Bellan [59] devolatilization scheme and drying kinetics.

Reaction	Cellulose	Hemicellulose	Lignin
k_1	$2.80 \times 10^{19}\exp(-242.4/RT)$	$2.10 \times 10^{16}\exp(-186.7/RT)$	$9.60 \times 10^{8}\exp(-107.6/RT)$
k_2	$3.28 \times 10^{14}\exp(-196.5/RT)$	$8.75 \times 10^{15}\exp(-202.4/RT)$	$1.50 \times 10^{9}\exp(-143.8/RT)$
k_3	$1.30 \times 10^{10}\exp(-150.5/RT)$	$2.60 \times 10^{11}\exp(-145.7/RT)$	$7.70 \times 10^{6}\exp(-111.4/RT)$
X	0.35	0.60	0.75
Drying for bound and free water: $5.13 \times 10^{8}\exp(-88/RT)$			

$$\frac{d\rho_{V,i}}{dt} = -k_1\rho_{V,i} \tag{44}$$

$$\frac{d\rho_{A,i}}{dt} = k_1\rho_{V,i} - k_2\rho_{A,i} - k_3\rho_{A,i} \tag{45}$$

$$\frac{d\rho_{tar,i}}{dt} = k_2\rho_{A,i} \tag{46}$$

$$\frac{d\rho_{gas,i}}{dt} = (1 - X_i)k_3\rho_{A,i} \quad (47)$$

$$\frac{d\rho_{char,i}}{dt} = X_i k_3 \rho_{A,i} \quad (48)$$

The products of the reaction scheme in Figure 1d are tar, char, and volatile gas. The kinetics parameter for each lignocellulosic decomposition is given in Table 7 and the profile of decomposition is summarized in Figure 25. Different devolatilization temperature leads to different composition of tar, volatile gas and char as presented in Figure 25a-c for devolatilization of cellulose, hemicellulose and lignin respectively. This conclusion is consistent with earlier researchers' results in other biomass systems [39,68].

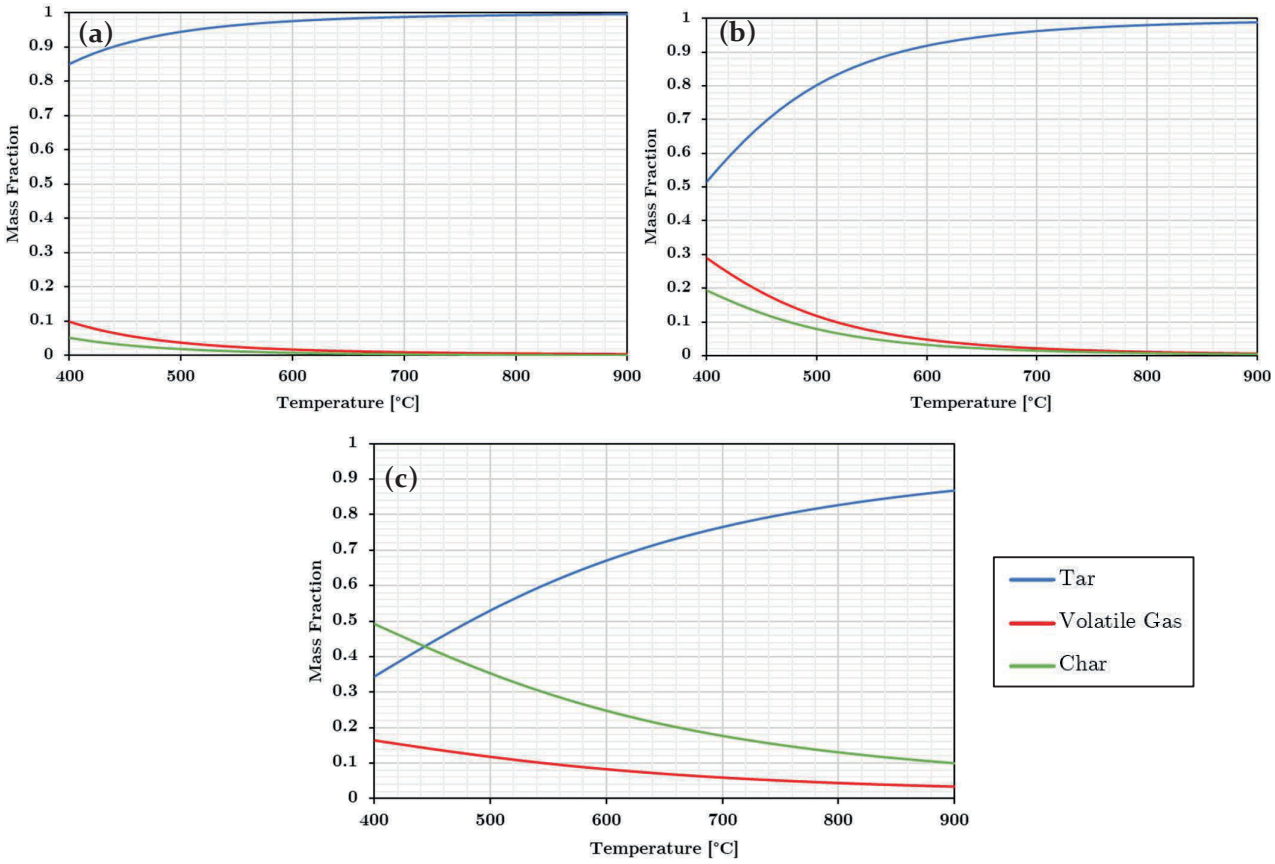

Figure 25. Mass fraction distribution of tar, volatile gas, and char from isothermal devolatilization of (a) cellulose, (b) hemicellulose and (c) lignin

In the current study, tar is further degraded into volatile gas, and volatile gas is assumed to be a combination of light gases. The mass and energy balance concepts are used to calculate the composition of each gas, with the assumptions mentioned below:

1) Chemical formula of cellulose, hemicellulose and lignin are defined as $C_6H_{10}O_5$, $C_5H_8O_5$, and $C_{11}H_{10}O_{3.2}$ respectively.
2) Tar chemical formulas are defined similarly with the original lignocellulosic compound.
3) Tar is decomposed further into volatile gas at instant rate.
4) Volatile gas consists of CO_2, CO, H_2, H_2O, O_2, CH_4, C_2H_4, and C_2H_2.
5) Char from cellulose, hemicellulose and lignin is defined as pure carbon.

6) Total heat of combustion or low calorific value can be calculated as the combination of heat of char combustion, heat of gas combustion, and heat of biomass decomposition as depicted in Eq.(49).

$$LCV = \left(x\,\Delta H^0_{f,CO_2} + \frac{y}{2}\Delta H^0_{f,H_2O}\right) + \left(GCV + \frac{y}{2}\,\Delta H_{evap}\right) = \dot{Q}_{char\ combustion} + \dot{Q}_{gas\ combustion} + \dot{Q}_{decomposition} \quad (49)$$

7) Heat of gas combustion can be calculated as sum of exothermic heat of reaction of R.4 to R.8.

$$C_2H_4 + 3\,O_2 \rightarrow 2\,CO_2 + 2\,H_2O \quad (R.4)$$
$$C_2H_2 + 2.5\,O_2 \rightarrow 2\,CO_2 + H_2O \quad (R.5)$$
$$CH_4 + 2\,O_2 \rightarrow CO_2 + 2\,H_2O \quad (R.6)$$
$$CO + 0.5\,O_2 \rightarrow CO_2 \quad (R.7)$$
$$H_2 + 0.5\,O_2 \rightarrow H_2O \quad (R.8)$$

Based on the aforementioned assumptions, the average mass fraction of gaseous compounds produced by tar and volatile gas conversion in the devolatilization temperature range of 400 to 900°C is calculated and reported in Table 8.

Table 8. Gas mixture composition from tar decomposition and average gas mixture from volatile gas decomposition within temperature range of 400 to 900°C (in mass fraction).

Gaseous Compound	Cellulose		Hemicellulose		Lignin	
	Volatile gas	Tar	Volatile gas	Tar	Volatile gas	Tar
CO	0.10	0.52	$6.90.10^{-3}$	0.26	$4.65.10^{-2}$	0.46
CO_2	0.22	-	0.20	0.32	$7.56.10^{-2}$	-
O_2	-	-	$2.02.10^{-4}$	-	-	-
H_2O	0.61	0.22	0.79	0.18	0.76	-
H_2	$1.66.10^{-2}$	-	$6.01.10^{-4}$	-	$5.31.10^{-2}$	-
CH_4	$2.60.10^{-2}$	-	$1.15.10^{-4}$	-	$2.31.10^{-2}$	-
C_2H_4	$2.78.10^{-2}$	0.26	-	0.24	$2.08.10^{-2}$	0.16
C_2H_2	-	-	-	-	$2.08.10^{-2}$	0.38

Lignin is the primary contributor of C_2H_2 gas, which is one of the primary precursors of soot particles. This is consistent with the results of prior studies [79,106] which revealed that lignin contributes more to soot production in biomass combustion systems. The average mass percentage of pyrolytic water obtained is around 15%, which coincides with experimental results reported in prior studies on rapid pyrolysis of coconut shells [107]. The distribution of gaseous compounds during devolatilization is accounted for in the transient CFD simulation to allow accurate prediction of gas phase combustion and, as a result, soot formation and reduction.

5.2.2. Transient CFD simulation setup

Simulation setup for transient CFD simulation has been thoroughly discussed in **Paper IV**. In the time-resolved CFD study, the same furnace geometry and mesh were utilized as in the steady CFD analysis. The biomass layer is divided into three rows in the current analysis,

with the thickness and length of each row set to 5 and 40 mm, respectively. In order for the biomass layer to absorb incoming radiation appropriately, 0.5 mm layers are built on top of the biomass and char layers. Using a user-defined function (UDF) code, the radiation heat transfer is calculated in this thin layer. This layer served as a radiation heat receiver, transferring heat to the biomass and char layers through conduction. User-defined functions (UDFs) were also used in the grate to precisely replicate different flow restriction properties along the grate.

The $k-\omega$ turbulence model was used in conjunction with the eddy dissipation concept (EDC) model for the volumetric gas reaction (R.4 to R.8). Table 2 in **Paper IV** summarizes the biomass thermal characteristics used in the current simulation. The initial state of the biomass and char layers in the transient simulation is also shown in Table 2 in **Paper IV**. Six different gaseous compounds were introduced to the freeboard from biomass layer i.e., CO_2, CO, H_2, H_2O, O_2, CH_4, C_2H_4, as mass sources. The pyrolysis product prediction was used to determine the gas composition. Meanwhile, char has accumulated over several cycles and the reaction was simplified to be a constant carbon combustion over a minute cycle. The gaseous components reacted in the gas phase following reaction schemes R.4 to R.8. Boundary conditions for inlet, outlet and walls were defined similarly as steady simulation.

5.2.3. Soot formation and reduction model

The two-step Tesner model [66] was used to predict soot formation and reduction in the combustion chamber. It predicts the development of nuclei and soot particles using two governing equations defined by Eqs. (50) to (51).

$$\frac{\partial \rho b_{nuc}^{*}}{\partial t}+\nabla\cdot(\rho\vec{v}b_{nuc}^{*})=\nabla\cdot\left(\frac{\mu_t}{\sigma_{nuc}}\nabla b_{nuc}^{*}\right)+R_{nuc}^{*} \tag{50}$$

$$\frac{\partial \rho Y_{soot}}{\partial t}+\nabla\cdot(\rho\vec{v}Y_{soot})=\nabla\cdot\left(\frac{\mu_t}{\sigma_{soot}}\nabla Y_{soot}\right)+R_{soot} \tag{51}$$

5.2.4. Time resolved CFD and experimental results

The simulation result of PM_{10} and CO_2 in the furnace are convoluted using the respective RTD as presented in Figure 7. Figure 26 show the transient measurement within one minute, as well as the original and convoluted signals from CFD analysis for PM_{10}, CO_2, and temperature. The results of CFD simulations from two different realizations are shown to ensure that the simulation results over one minute are stable for both realizations.

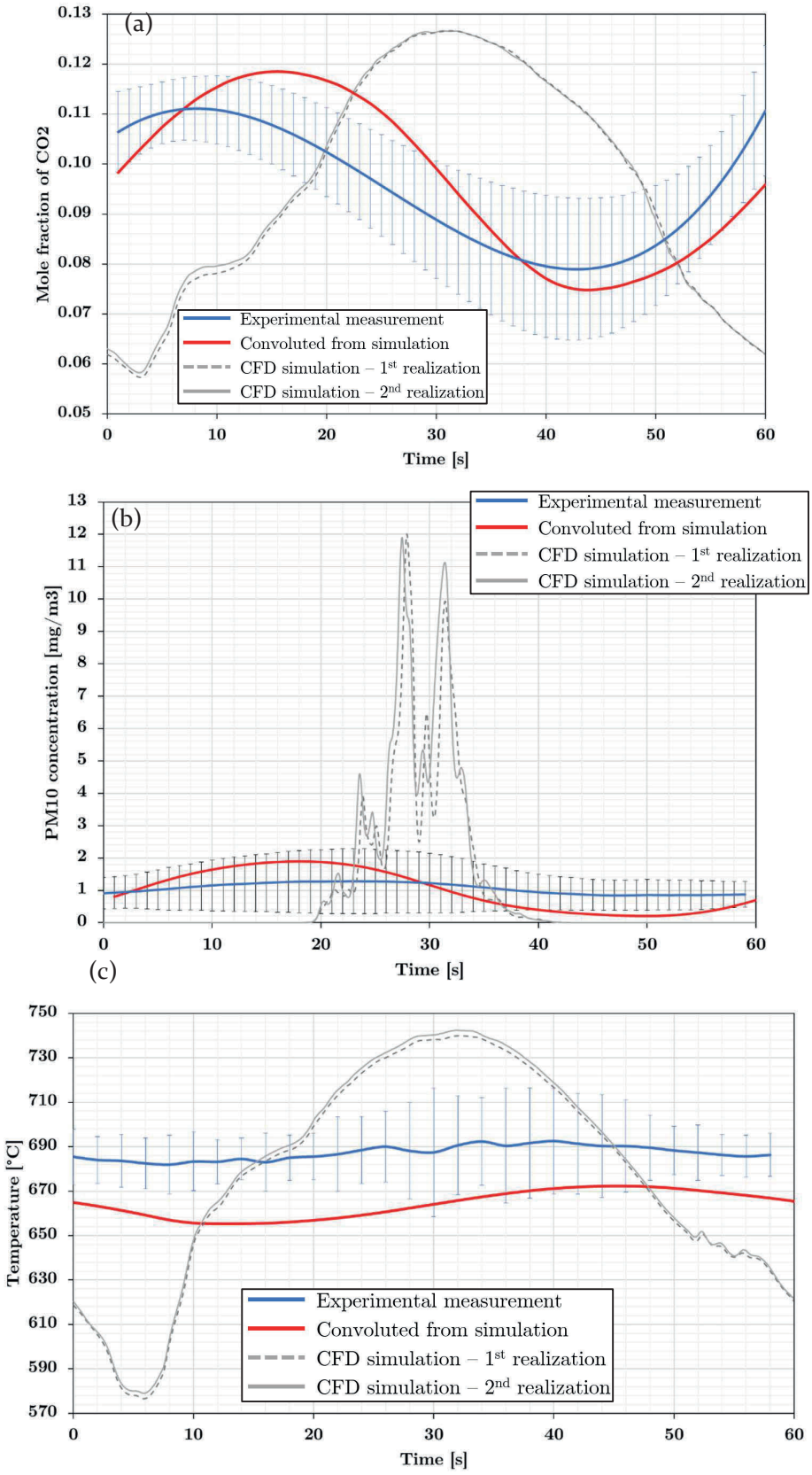

Figure 26. Transient measurement and simulation results for (a) CO_2 concentration, (b) PM concentration, and (c) chimney temperature.

Taking the statical error bars into account, the convoluted CFD results correlates fairly well with the measurement data reported in Figure 26. It also underlines the significance of signal convolution in preventing data misinterpretation. Temperature has a slight offset due to problems in building an accurate thermocouple geometry and uncertainty in the exact material characteristics of the thermocouple shield. Based on Figure 26, maximum PM occurs at 30 seconds in the region with the highest CO_2 levels. This indicates a lack of oxygen during that period, which could have hindered soot combustion in the freeboard.

The CFD simulation results show that the current CFD model is capable of predicting the global behavior of biomass combustion and soot emission over a one-minute combustion cycle. The average CO_2 mole fraction and PM_{10} concentration from a CFD simulation of a one-minute combustion cycle differ by 0.51% and 10.25%, respectively, compared to the average experimental data. There are minor differences in the dynamics of the CO_2 and PM profiles. This can be due to simulation works rely only on one specific distribution of biomass over the grate. The distribution of biomass above the grate determines the heat transfer rate as well as the rate of drying and devolatilization.

5.2.5. Influence of combustion on soot emissions

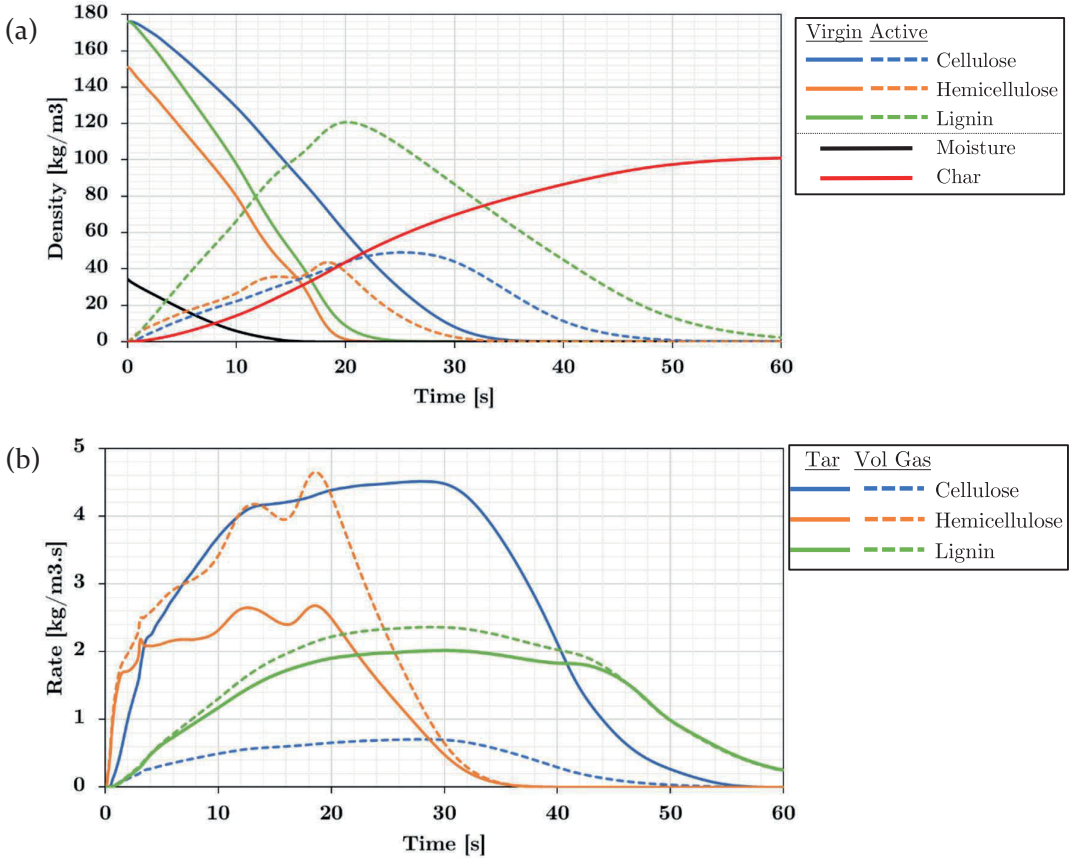

Figure 27. CFD simulation results for (a) conversion of the virgin and active lignocellulosic components and (b) volatile gas and tar formation rate originating from the three lignocellulosic components.

Figure 27a shows the conversion of several lignocellulosic components during a one-minute combustion cycle. The drying process begins when new biomass is loaded onto the grate and the bottom parts of the biomass that are in contact with the hot char layer experience early drying. This is the first layer to reach devolatilization temperature, which is roughly 350°C. However, once the flame is formed, heat propagation occurs more intensely at the top layer of biomass due to increased radiation intensity.

Figure 27b reveals that lignin produces roughly the same percentage of tar and volatile gas as cellulose and hemicellulose, and the conversion occurs at a later period than cellulose and hemicellulose. ln conjunction with Figure 26a, one can exclude hemicellulose contribution to soot formation because it has been totally devolatilized before maximum soot concentration is reached. Acetylene which is known as the main precursor of soot in biomass combustion system [58] emphasizes bigger contribution of lignin to soot emission than cellulose. This is supported by the major fraction of acetylene released from lignin decomposition as summarized in Table 8. Moreover, Figure 28 highlights an overlapping period between soot concentration and acetylene released from lignin.

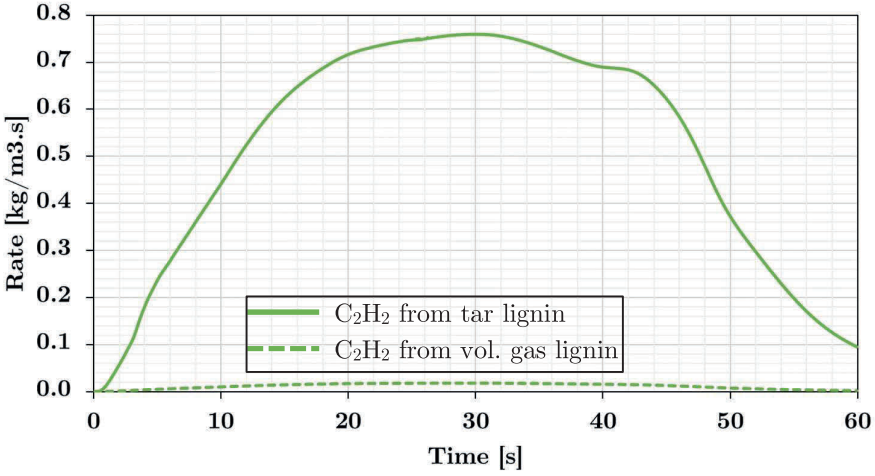

Figure 28. Formation rate of acetylene (C_2H_2) from lignin decomposition based on simulations.

CFD simulations can be used to learn more about the mechanisms of soot formation and reduction within the combustion chamber. According to Figure 29, soot formation and reduction occur concurrently during the combustion cycle. Calculations based on the volume integrated rate of soot formation and reduction during the one-minute combustion cycle shows that 99.3% of all soot formed in the combustion chamber is reduced before the exhaust gas leaves the furnace.

The presence of acetylene as a soot precursor, the temperature level, and the availability of oxygen in the freeboard, influence soot formation and reduction. Based on Figure 29, soot formation is enhanced by the availability of acetylene and temperature rise, as seen in the 15-second interval. However, due to the high concentration of remaining oxygen, the rate of soot reduction is accelerated. Between 20 and 40 seconds, the restricted supply of oxygen begins to induce an increase in soot emission. Following this interval, the soot concentration is seen to be decreased since both hemicellulose and cellulose have been totally devolatilized which increases the oxygen concentration in the freeboard.

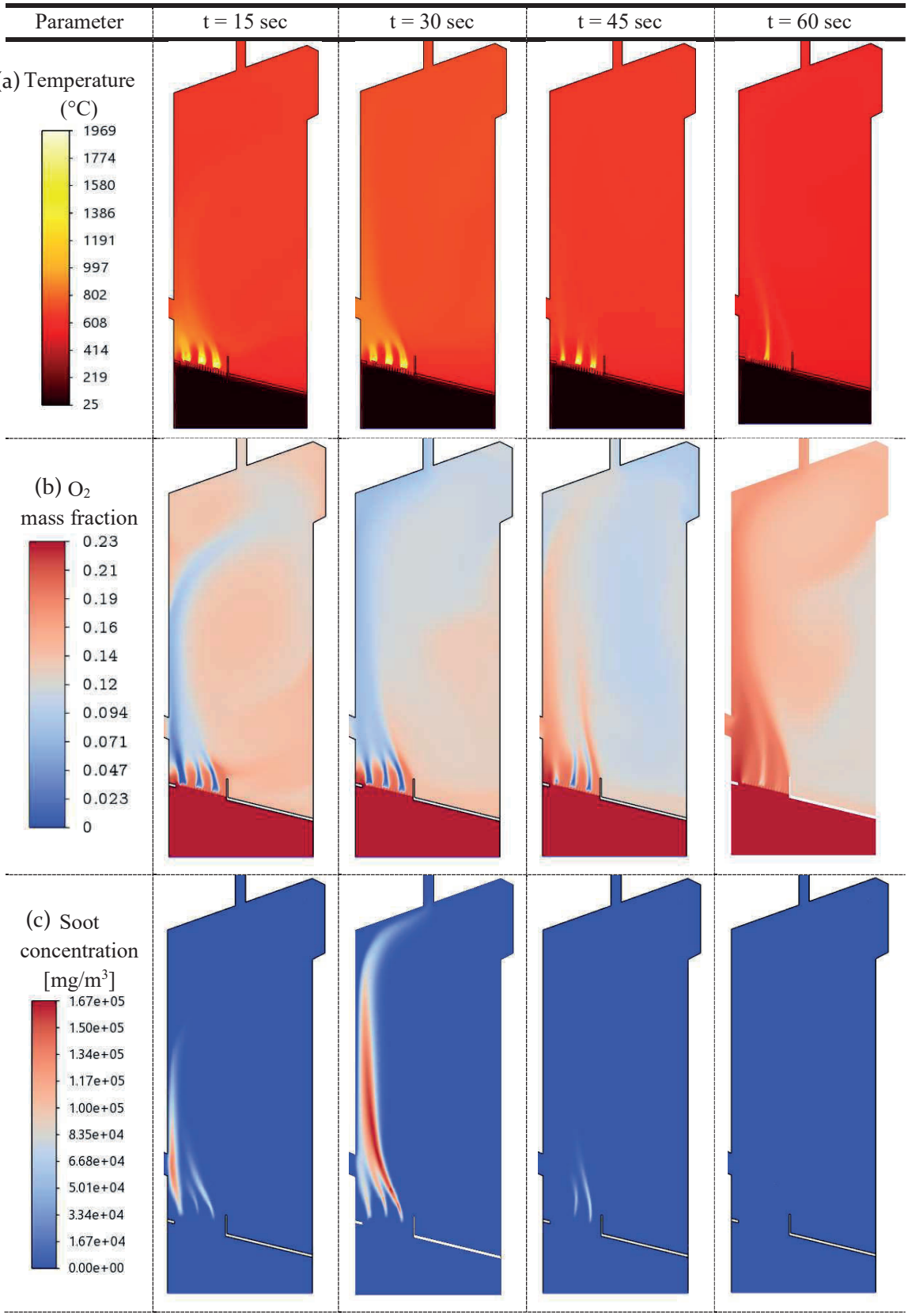
Parameter
t = 15 sec
t = 30 sec
t = 45 sec
t = 60 sec
(a) Temperature (°C)
1969
1774
1580
1386
1191
997
802
608
414
219
25
(b) O2 mass fraction
0.23
0.21
0.19
0.16
0.14
0.12
0.094
0.071
0.047
0.023
0
(c) Soot concentration [mg/m3]
1.67e+05
1.50e+05
1.34e+05
1.17e+05
1.00e+05
8.35e+04
6.68e+04
5.01e+04
3.34e+04
1.67e+04
0.00e+00

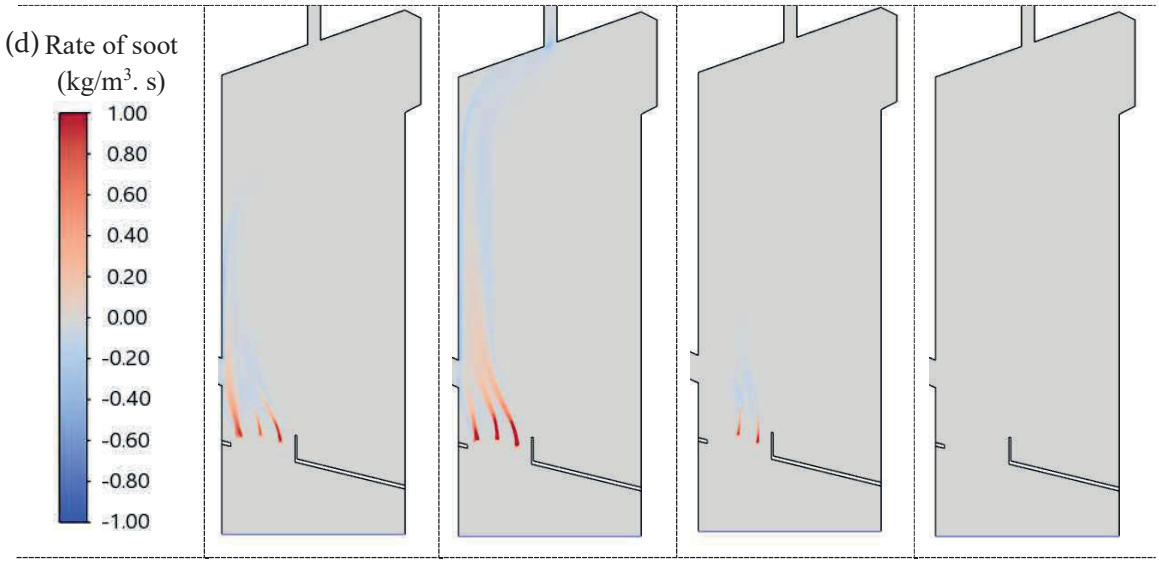

Figure 29. Contour plots of (a) temperature, (b) O_2 mass fraction, (c) soot concentration, (d) rate of soot formation and reduction over one minute combustion cycle.

6. Summary and Future Outlook

6.1. Summary

This study aims to develop knowledge of the formation and reduction of PM in residual biomass combustion by utilizing modelling, simulation, and experimental techniques. The multiscale modelling and simulation analysis involves improvement in particle model for biomass combustion and PM emission prediction in biomass furnace. The developed models are validated against observation from experimental facility to ensure model accuracy and reliability.

A new model for single particle pyrolysis and combustion was developed using the orthogonal colocation method. The discretization scheme combined with a comprehensive physicochemical particle model provides improvement in heat and mass transfer rates inside and at the particle surface. The intraparticle temperature gradient, as well as particle mass and size developments, were predicted accurately in comparison to data from particle pyrolysis and combustion experiments for different particle moisture levels and shapes. Furthermore, the current model improved prior models (mesh- and interface-based models) by being numerically more stable and computationally more efficient.

An improvement in the particle model is also achieved by quantifying and studying mass transfer to and from spheres by high resolved CFD simulations. The inclusion of Stefan flow significantly increases the mass transport's film thickness, while a marginal difference in film thickness between even and uneven Stefan flow is observed. The Stefan flow analysis demonstrated that the rate of mass transfer may be expressed as a function of the nominal Sherwood i.e., Sh without Stefan flow, a dimensionless number $An = \frac{u_s d}{D}$ and the change in film thickness (using adjusted Reynolds number). It is concluded that the new model allows significant improvements compared to commonly used models over the entire range of Re, An and Sc numbers.

A lab-scale grate-fired furnace is successfully designed and equipped with on-line sensors to study emissions of particulate matter originating from residual biomass combustion at different combustion conditions. To accurately measure the key combustion parameters, various measurement techniques have been developed and utilized in the experimental facility. The experimental results agree with the current understanding of PM emission under different combustion conditions, i.e., residence time, temperature of combustion and air/fuel ratio, significantly affect the emissions. By increasing the residence time, primary air temperature, and air/fuel ratio, PM_{10} emissions for the range of experimental explored conditions are further reduced by up to 80% compared to the nominal conditions.

A steady CFD analysis of biomass combustion in a grate fired furnace is carried out to predict global behavior of biomass combustion and provide a better understanding of several parameters that are difficult to obtain directly from experiment, e.g., flow field, gas temperature and residence time distributions, and particle history data. The Arrhenius kinetic parameters of PM_{10} reduction in the furnace are successfully calculated by combining experimental and CFD simulation data i.e., 23.1 (s^{-1}) for the rate constant at reference temperature (900°C) and 126.2 ($kJ.mol^{-1}$) for the activation energy.

The improvement of steady CFD analysis i.e., the time resolved CFD simulation, provided better understanding of the influence of combustion parameters and lignocellulosic components in the biomass, to the PM formation and reduction in the combustion system. To account for the hydrodynamic dispersion effect that occurs in pipe systems and sensors, the transient CFD results are convoluted. The convoluted results were compared with the experimental observations to ensure the accuracy of the CFD model. According to CFD analysis, the presence of soot precursors from lignin decomposition, i.e., acetylene, and high temperature in the freeboard promotes an increased rate of soot formation. Meanwhile, oxygen availability has emerged as the most important factor in soot reduction. CFD calculations show that 99.3% of the soot generated in the freeboard is burnt before the exhaust gas exits the chimney.

6.2. Future Outlook

The results from this study can inspire further works related to optimization of biomass combustion operating conditions and furnace design. The CFD model has potential applications to evaluate different furnace designs and operating conditions which can provide high conversion of energy while maintaining low level of PM emission. Along with the improvements that can be made in the experimental facility, such as the observation of additional gaseous components, the CFD model may be upgraded to accommodate the prediction of other emissions, such as NOx, SOx, PAH, and so on.

The use of orthogonal collocation may help increase the efficiency of CFD simulation. The present CFD model depends on a rather dense mesh in the biomass particle layers, which contributes to the high computing power requirement. The utilization of the developed particle model is expected to reduce computational power, particularly in 3D simulations and/or larger furnaces, such as biomass fueled boilers for electricity production. In CFD modelling, the Sherwood number correction due to Stefan flow may also be included as particle and bed sub-grid models. The utilization of this sub-grid model is expected to improve the accuracy of simulations while maintaining low computational power.

Nomenclature

A	=	Orthogonal collocation coefficient for first derivative [-]
An	=	Andersson number [-]
A_p	=	Particle surface area [m^2]
a	=	Geometry coefficient [-]
B	=	Orthogonal collocation coefficient for second derivative [-]
β	=	Shrinking and swelling factor [-]
b^*_{nuc}	=	Normalized radical nuclei concentration (number of particles $\times 10^{-15}$ kg^{-1})
C	=	Concentration [$mg.m^{-3}$ or %vol or kg m^{-3}]
Cp	=	Specific heat capacity [J kg^{-1} K^{-1}]
D	=	Orthogonal collocation coefficient [-]
D_A	=	Diffusivity [m^2 s^{-1}]
d	=	Orthogonal collocation coefficient or Coefficient for cubic hermite interpolation [-]
d_p	=	Diameter particle [m]
E	=	Residence time distribution [s^{-1}]
E_a	=	Activation energy [kJ mol^{-1}]
$\vec{g}$	=	Gravitational forces [m s^{-2}]
$\vec{F}$	=	External body forces [kg m^{-2} s^{-2}]
GCV	=	Gross calorific value [kJ/kg]
h	=	Convective heat transfer coefficient [W m^{-2} K^{-1}]
ΔH	=	Enthalpy [kJ/mol]
ΔH_f^0	=	Enthalpy of formation at reference temperature [kJ/mol]
i	=	Collocation point [-]
k	=	Reaction rate constant [s^{-1}]
$\vec{J_i}$	=	Diffusion flux of species i [kg m^{-3} s^{-1}]
LCV	=	Lower calorific value [kJ/kg]
N	=	Total collocation points [-]
Q	=	Orthogonal collocation coefficient [-]
R	=	Radius [m]
Re	=	Reynold number [-]
R_g	=	Ideal gas constant [kJ mol^{-1} K^{-1}]
R_i	=	Net rate of production of species i [kg m^{-3} s^{-1}]
R^*_{nuc}	=	Normalized net rate of nuclei generation (number of particles $\times 10^{-15}$ m^{-3} s^{-1})
R_{soot}	=	Net rate of soot generation [kg $m^{-3}s^{-1}$]
r	=	Local radius [m]
$\dot{r}$	=	Reaction rate [kg m^{-3} s^{-1}] / [kg m^{-2} s^{-1}]
Sh	=	Sherwood number [-]
Sc	=	Schmidt number [-]
S_i	=	The rate of creation of species i by addition from the dispersed phase plus any user-defined sources [kg m^{-3} s^{-1}]
S_m	=	Mass added to continuous phase from the dispersed second phase and any user-defined sources [kg m^{-3} s^{-1}]
T	=	Temperature [K]
t	=	Time [s]
u_s	=	Velocity at the surface [m s^{-1}]
V_p	=	Volume [m^3]
W	=	Weighting factor in shifted Legendre polynomials [-] or Width [m]
x	=	Dimensionless coordinate [-]
Y_i	=	Local mass fraction of species i [-]
Y_{soot}	=	Mass fractions of soot [-]

y_{O_2}	=	Oxygen mass fraction [-]

Greek letters

ε	=	Porosity [-] / Emmisivity [-]
ρ	=	Density or species concentration [kg m^{-3}]
ω	=	Stefan-Boltzmann constant [W m^{-2} K^{-4}]
λ_{eff}	=	Thermal conductivity [W m^{-1} K^{-1}]
σ_{nuc}	=	Turbulent Prandtl number for nuclei transport [-]
σ	=	Stefan-Boltzmann constant [W m^{-2} K^{-4}]
$\bar{\bar{\tau}}$	=	Stress tensor [N m^{-2}]

References

[1] Wang X, Hu Z, Adeosun A, Liu B, Ruan R, Li S, et al. Particulate matter emission and K/S/Cl transformation during biomass combustion in an entrained flow reactor. Journal of the Energy Institute 2018;91:835–44.

[2] Anca-Couce A. Reaction mechanisms and multi-scale modelling of lignocellulosic biomass pyrolysis. Progress in Energy and Combustion Science 2016;53:41–79.

[3] 2030 Energy Strategy - European Commission n.d. https://ec.europa.eu/energy/en/topics/energy-strategy-and-energy-union/2030-energy-strategy (accessed December 15, 2018).

[4] Sweden to reach its 2030 renewable energy target this year | World Economic Forum n.d. https://www.weforum.org/agenda/2018/07/sweden-to-reach-its-2030-renewable-energy-target-this-year/ (accessed December 15, 2018).

[5] Biomass explained - U.S. Energy Information Administration (EIA) n.d. https://www.eia.gov/energyexplained/biomass/ (accessed September 23, 2020).

[6] Final Report | The Contribution of Biomass Combustion to Ambient Fine Particle Concentrations in the United States | Research Project Database | Grantee Research Project | ORD | US EPA n.d. https://cfpub.epa.gov/ncer_abstracts/index.cfm/fuseaction/display.abstractDetail/abstract/104/report/F (accessed June 30, 2020).

[7] Chen J, Li C, Ristovski Z, Milic A, Gu Y, Islam MS, et al. A review of biomass burning: Emissions and impacts on air quality, health and climate in China. Science of the Total Environment 2017;579:1000–34.

[8] Puxbaum H, Caseiro A, Sánchez-Ochoa A, Kasper-Giebl A, Claeys M, Gelencsér A, et al. Levoglucosan levels at background sites in Europe for assessing the impact of biomass combustion on the European aerosol background. Journal of Geophysical Research Atmospheres 2007;112:1–11.

[9] WHO | Ambient air pollution n.d. https://www.who.int/gho/phe/outdoor_air_pollution/en/#:~:text=Particulate%20matter%20pollution%20is%20an,countries%20disproportionately%20experience%20this%20burden.&text=In%202016%2C%20indoor%20and%20outdoor,one%20in%20nine%20deaths%20globally. (accessed August 12, 2020).

[10] Vicente ED, Alves CA. An overview of particulate emissions from residential biomass combustion. Atmospheric Research 2018;199:159–85.

[11] Josephson AJ, Linn RR, Lignell DO. Modeling soot formation from solid complex fuels. Combustion and Flame 2018;196:265–83.

[12] Sippula O, Hytönen K, Tissari J, Raunemaa T, Jokiniemi J. Effect of wood fuel on the emissions from a top-feed pellet stove. Energy and Fuels 2007;21:1151–60.

[13] Ratcliff MA, Windom B, Fioroni GM, st. John P, Burke S, Burton J, et al. Impact of ethanol blending into gasoline on aromatic compound evaporation and particle emissions from a gasoline direct injection engine. Applied Energy 2019;250:1618–31.

[14] Yang J, Ma Y, Fu J, Shu J, Liu J. Parametric study of gasoline properties on combustion characteristics of gasoline compression engines using reaction kinetics simulation and density-based global sensitivity analysis. Applied Energy 2019;255:113858.

[15] Qian Y, Li Z, Yu L, Wang X, Lu X. Review of the state-of-the-art of particulate matter emissions from modern gasoline fueled engines. Applied Energy 2019;238:1269–98.

[16] Wang B, Mosbach S, Schmutzhard S, Shuai S, Huang Y, Kraft M. Modelling soot formation from wall films in a gasoline direct injection engine using a detailed population balance model. Applied Energy 2016;163:154–66.

[17] Trandafilović L v., Mihai O, Woo J, Leistner K, Stenfeldt M, Olsson L. A kinetic model for SCR coated particulate filters—Effect of ammonia-soot interactions. Applied Catalysis B: Environmental 2019;241:66–80.

[18] Soltani S, Andersson R, Andersson B. The effect of exhaust gas composition on the kinetics of soot oxidation and diesel particulate filter regeneration. Fuel 2018;220:453–63.

[19] Ström H, Sjöblom J, Kannan AS, Ojagh H, Sundborg O, Koegler J. Near-wall dispersion, deposition and transformation of particles in automotive exhaust gas aftertreatment systems. International Journal of Heat and Fluid Flow 2018;70:171–80.

[20] Mihai O, Stenfeldt M, Olsson L. The effect of changing the gas composition on soot oxidation over DPF and SCR-coated filters. Catalysis Today 2018;306:243–50.

[21] Chen CY, Lee WJ, Wang LC, Chang YC, Yang HH, Young LH, et al. Impact of high soot-loaded and regenerated diesel particulate filters on the emissions of persistent organic pollutants from a diesel engine fueled with waste cooking oil-based biodiesel. Applied Energy 2017;191:35–43.

[22] Zhu M, Setyawan HY, Zhang Z, Zhang D. Effect of n-butanol addition on the burning rate and soot characteristics during combustion of single droplets of diesel–biodiesel blends. Fuel 2020;265:117020.

[23] Fletcher TH, Ma J, Rigby JR, Brown AL, Webb BW. Soot in coal combustion systems. Progress in Energy and Combustion Science 1997;23:283–301.

[24] Morris WJ, Yu D, Wendt JOL. Soot, unburned carbon and ultrafine particle emissions from air- and oxy-coal flames. Proceedings of the Combustion Institute 2011;33:3415–21.

[25] Zhuo JK, Li SQ, Yao Q, Song Q. The progressive formation of submicron particulate matter in a quasi one-dimensional pulverized coal combustor. Proceedings of the Combustion Institute 2009;32 II:2059–66.

[26] Black DL, McQuay MQ. Particle characteristics in the radiant section of a coal-fired utility boiler. Combustion Science and Technology 1998;132:37–74.

[27] Bäckström D, Johansson R, Andersson K, Johnsson F, Clausen S, Fateev A. Measurement and modeling of particle radiation in coal flames. Energy and Fuels, vol. 28, 2014, p. 2199–210.

[28] Khatri D, Gopan A, Yang Z, Adeosun A, Axelbaum RL. Characterizing early stage sub-micron particle formation during pulverized coal combustion in a flat flame burner. Fuel 2019;258:115995.

[29] Bäckström D, Gall D, Pushp M, Johansson R, Andersson K, Pettersson JBC. Particle composition and size distribution in coal flames - The influence on radiative heat transfer. Experimental Thermal and Fluid Science 2015;64:70–80.

[30] McConnell J, Sutherland JC. Assessment of various tar and soot treatment methods and a priori analysis of the steady laminar flamelet model for use in coal combustion simulation. Fuel 2020;265:116775.

[31] Niksa S. Predicting ultimate soot yields from any coal. Proceedings of the Combustion Institute 2019;37:2757–64.

[32] Ström H, Thunman H. CFD simulations of biofuel bed conversion: A submodel for the drying and devolatilization of thermally thick wood particles. Combustion and Flame 2013;160:417–31.

[33] Ström H, Thunman H. A computationally efficient particle submodel for CFD-simulations of fixed-bed conversion. Applied Energy 2013;112:808–17.

[34] Company B& W. Steam : its generation and use. 38th ed. New York : Babcock & Wilcox; 1972.

[35] Bryden KM, Hagge MJ. Modeling the combined impact of moisture and char shrinkage on the pyrolysis of a biomass particle☆. Fuel 2003;82:1633–44.

[36] Lu H, Robert W, Peirce G, Ripa B, Baxter LL. Comprehensive study of biomass particle combustion. Energy and Fuels 2008;22:2826–39.

[37] Khodaei H, Yeoh GH, Guzzomi F, Porteiro J. A CFD-based comparative analysis of drying in various single biomass particles. Applied Thermal Engineering 2018;128:1062–73.

[38] Haberle I, Skreiberg Ø, Łazar J, Haugen NEL. Numerical models for thermochemical degradation of thermally thick woody biomass, and their application in domestic wood heating appliances and grate furnaces. Progress in Energy and Combustion Science 2017;63:204–52.

[39] Haberle I, Haugen NEL, Skreiberg Ø. Drying of Thermally Thick Wood Particles: A Study of the Numerical Efficiency, Accuracy, and Stability of Common Drying Models. Energy and Fuels 2017;31:13743–60.

[40] Nugraha MG, Saptoadi H, Hidayat M, Andersson B, Andersson R. Particle modelling in biomass combustion using orthogonal collocation. Applied Energy 2019;255:113868.

[41] Popescu F, Mahu R, Ion I v., Rusu E. A Mathematical Model of Biomass Combustion Physical and Chemical Processes. Energies (Basel) 2020;13:6232.

[42] Josephson AJ, Hopkins EM, Lignell DO, Linn RR. Reduction of a detailed soot model for simulations of pyrolysing solid fuels. Combustion Theory and Modelling 2020;24:15–40.

[43] Neves D, Thunman H, Matos A, Tarelho L, Gómez-Barea A. Characterization and prediction of biomass pyrolysis products. Progress in Energy and Combustion Science 2011;37:611–30.

[44] Wurzenberger JC, Wallner S, Raupenstrauch H, Khinast JG. Thermal conversion of biomass: Comprehensive reactor and particle modeling. AIChE Journal 2002;48:2398–411.

[45] Porteiro J, Míguez JL, Granada E, Moran JC. Mathematical modelling of the combustion of a single wood particle. Fuel Processing Technology 2006;87:169–75.

[46] Hagge MJ, Bryden KM. Modeling the impact of shrinkage on the pyrolysis of dry biomass. Chemical Engineering Science 2002;57:2811–23.

[47] Grønli MG, Melaaen MC. Mathematical Model for Wood PyrolysisComparison of Experimental Measurements with Model Predictions. Energy & Fuels 2000;14:791–800.

[48] Bryden KM, Ragland KW, Rutland CJ. Modeling thermally thick pyrolysis of wood. Biomass and Bioenergy 2002;22:41–53.

[49] Biswas AK, Umeki K. Simplification of devolatilization models for thermally-thick particles: Differences between wood logs and pellets. Chemical Engineering Journal 2015;274:181–91.

[50] Koufopanos CA, Lucchesi A, Maschio G. Kinetic modelling of the pyrolysis of biomass and biomass components. The Canadian Journal of Chemical Engineering 1989;67:75–84.

[51] Bradbury AGW, Sakai Y, Shafizadeh F. A kinetic model for pyrolysis of cellulose. Journal of Applied Polymer Science 1979;23:3271–80.

[52] Agrawal RK. Kinetics of reactions involved in pyrolysis of cellulose I. The three reaction model. The Canadian Journal of Chemical Engineering 1988;66:403–12.

[53] Fitzpatrick EM, Bartle KD, Kubacki ML, Jones JM, Pourkashanian M, Ross AB, et al. The mechanism of the formation of soot and other pollutants during the co-firing of coal and pine wood in a fixed bed combustor. Fuel 2009;88:2409–17.

[54] Fitzpatrick EM, Jones JM, Pourkashanian M, Ross AB, Williams A, Bartle KD. Mechanistic aspects of soot formation from the combustion of pine wood. Energy and Fuels 2008;22:3771–8.

[55] Růžičková J, Kucbel M, Raclavská H, Švédová B, Raclavský K, Juchelková D. Comparison of organic compounds in char and soot from the combustion of biomass in boilers of various emission classes. Journal of Environmental Management 2019;236:769–83.

[56] Boutin O, Ferrer M, Lédé J. Radiant flash pyrolysis of cellulose - Evidence for the formation of short life time intermediate liquid species. Journal of Analytical and Applied Pyrolysis 1998;47:13–31.

[57] Liu Q, Wang SR, Wang KG, Guo XJ, Luo ZY, Cen KF. Mechanism of formation and consequent evolution of active cellulose during cellulose pyrolysis. Wuli Huaxue Xuebao/ Acta Physico - Chimica Sinica 2008;24:1957–63.

[58] Conesa JA, Caballero JA, Marcilla A, Font R. Analysis of different kinetic models in the dynamic pyrolysis of cellulose. Thermochimica Acta 1995;254:175–92.

[59] Miller RS, Bellan J. A generalized biomass pyrolysis model based on superimposed cellulose, hemicellulose and lignin kinetics. Combustion Science and Technology 1997;126:97–137.

[60] Moilanen A, Saviharju K, Harju T. Steam Gasification Reactivities of Various Fuel Chars. Advances in Thermochemical Biomass Conversion 1993:131–41.

[61] di Blasi C. Combustion and gasification rates of lignocellulosic chars. Progress in Energy and Combustion Science 2009;35:121–40.

[62] Gómez MA, Porteiro J, Patiño D, Míguez JL. CFD modelling of thermal conversion and packed bed compaction in biomass combustion. Fuel 2014;117:716–32.

[63] Neves D, Thunman H, Matos A, Tarelho L, Gómez-Barea A. Characterization and prediction of biomass pyrolysis products. Progress in Energy and Combustion Science 2011;37:611–30.

[64] Fletcher TH, Kerstein AR, Pugmire RJ, Solum MS, Grant DM. Chemical Percolation Model for Devolatilization. 3. Direct Use of 13C NMR Data To Predict Effects of Coal Type. Energy and Fuels 1992;6:414–31.

[65] Lewis AD, Fletcher TH. Prediction of sawdust pyrolysis yields from a flat-flame burner using the CPD model. Energy and Fuels 2013;27:942–53.

[66] Horton SR, Mohr RJ, Zhang Y, Petrocelli FP, Klein MT. Molecular-Level Kinetic Modeling of Biomass Gasification. Energy and Fuels 2016;30:1647–61.

[67] Wang S, Dai G, Yang H, Luo Z. Lignocellulosic biomass pyrolysis mechanism: A state-of-the-art review. Progress in Energy and Combustion Science 2017;62:33–86.

[68] Collazo J, Porteiro J, Míguez JL, Granada E, Gómez MA. Numerical simulation of a small-scale biomass boiler. Energy Conversion and Management 2012;64:87–96.

[69] Bhuiyan AA, Naser J. Numerical modeling of Biomass co-combustion with pulverized coal in a small scale furnace. Procedia Engineering 2015;105:504–11.

[70] Farokhi M, Birouk M. A new EDC approach for modeling turbulence/chemistry interaction of the gas-phase of biomass combustion. Fuel 2018;220:420–36.

[71] Parente A, Malik MR, Contino F, Cuoci A, Dally BB. Extension of the Eddy Dissipation Concept for turbulence/chemistry interactions to MILD combustion. Fuel 2016;163:98–111.

[72] Farokhi M, Birouk M. Application of Eddy Dissipation Concept for Modeling Biomass Combustion, Part 1: Assessment of the Model Coefficients. Energy and Fuels 2016;30:10789–99.

[73] Kantová NČ, Sładek S, Jandačka J, Čaja A, Nosek R. Simulation of biomass combustion with modified flue gas tract. Applied Sciences (Switzerland) 2021;11:1–11.

[74] Farokhi M, Birouk M. Application of Eddy Dissipation Concept for Modeling Biomass Combustion, Part 2: Gas-Phase Combustion Modeling of a Small-Scale Fixed Bed Furnace. Energy and Fuels 2016;30:10800–8.

[75] MAGNUSSEN B. On the structure of turbulence and a generalized eddy dissipation concept for chemical reaction in turbulent flow 1981.

[76] Shiehnejadhesar A, Mehrabian R, Scharler R, Goldin GM, Obernberger I. Development of a gas phase combustion model suitable for low and high turbulence conditions. Fuel 2014;126:177–87.

[77] Kocbach Bølling A, Pagels J, Yttri K, Barregard L, Sallsten G, Schwarze PE, et al. Health effects of residential wood smoke particles: the importance of combustion conditions and physicochemical particle properties. Particle and Fibre Toxicology 2009;6:29.

[78] Sippula O, Hokkinen J, Puustinen H, Yli-Pirilä P, Jokiniemi J. Comparison of particle emissions from small heavy fuel oil and wood-fired boilers. Atmospheric Environment 2009;43:4855–64.

[79] Deng C, Liaw SB, Gao X, Wu H. Differences in soot produced from rapid pyrolysis of xylan, cellulose and lignin under pulverized-fuel conditions. Fuel 2020;265:116991.

[80] Bockhorn H. Soot Formation in Combustion Mechanisms and Models. vol. 59. Springer-Verlag; 1994.

[81] Sippula O. Fine particle formation and emission in biomass combustion. University of Eastern Finland, 2010.

[82] Kennedy IM. Models of soot formation and oxidation. Progress in Energy and Combustion Science 1997;23:95–132.

[83] Khan IM, Wang CHT, Langridge BE. Coagulation and combustion of soot particles in diesel engines. Combustion and Flame 1971;17:409–19.

[84] Tesner PA, Smegiriova TD, Knorre VG. Kinetics of dispersed carbon formation. Combustion and Flame 1971;17:253–60.

[85] Brookes SJ, Moss JB. Predictions of soot and thermal radiation properties in confined turbulent jet diffusion flames. Combustion and Flame 1999;116:486–503.

[86] Michelsen HA, Colket MB, Bengtsson PE, D'Anna A, Desgroux P, Haynes BS, et al. A review of terminology used to describe soot formation and evolution under combustion and pyrolytic conditions. ACS Nano 2020;14:12470–90.

[87] Frenklach M. Method of moments with interpolative closure. Chemical Engineering Science 2002;57:2229–39.

[88] Brohez S, Delvosalle C, Marlair G. A two-thermocouples probe for radiation corrections of measured temperatures in compartment fires. Fire Safety Journal 2004;39:399–411.

[89] Schwarz AD, Meyer J, Dittler A. Opportunities for Low-Cost Particulate Matter Sensors in Filter Emission Measurements. Chemical Engineering and Technology 2018;41:1826–32.

[90] Nova Fitness Co. L. Laser PM2.5 Sensor specification Product model: SDS011 Version: V1.3 2015:1–11.

[91] Masks and N95 Respirators | FDA n.d. https://www.fda.gov/medical-devices/personal-protective-equipment-infection-control/masks-and-n95-respirators (accessed February 18, 2020).

[92] 3M™ Particulate Respirator 8210, N95 160 EA/Case | 3M United States n.d. https://www.3m.com/3M/en_US/company-us/all-3m-products/~/3M-Particulate-Respirator-8210-N95-160-EA-Case/?N=5002385+3294780268&rt=rud (accessed February 12, 2020).

[93] FEI Quanta 650 SEM n.d. https://www.fei.com/products/sem/Quanta-SEM-for-Materials-Science/ (accessed March 20, 2020).

[94] Warnatz, J., Mass, U., Dibble RW. Combustion: Physical and Chemical Fundamentals, Modelling and Simulation, Experiments, Pollutant Formation. 4th ed. Berlin: Springer,; n.d.

[95] Kuenne G, Avdić A, Janicka J. Assessment of subgrid interpolation for the source term evaluation within premixed combustion simulations. Combustion and Flame 2017;178:225–56.

[96] Rice JR, Rice JR. Interpolation. Numerical Methods in Software and Analysis 1993:93–171.

[97] Michaelides EE. Particles, Bubbles And Drops - Their Motion, Heat and Mass Transfer. World Scientific Publishing Co. Pte. Ltd.; 2006.

[98] Haberle I, Haugen NEL, Skreiberg Ø. Combustion of Thermally Thick Wood Particles: A Study on the Influence of Wood Particle Size on the Combustion Behavior. Energy & Fuels 2018;32:6847–62.

[99] Inc. ANSYS. ANSYS FLUENT Theory Guide. Release 182 2013;15317:373–464.

[100] Ranz WE and MarshallWR. Evaporation from Drops. Chem Eng Prog 1952;48:173–80.

[101] Clift R, Grace JR, Weber ME. Bubbles, drops, and particles 2005.

[102] Froessling N. On the evaporation of falling drops. Army Biological Labs Frederick MD; 1968.

[103] Spalding DB (Dudley B. Combustion and mass transfer : a textbook with multiple-choice exercises for engineering students. Pergamon Press; 1979.

[104] Abramzon B, Sirignano WA. Droplet vaporization model for spray combustion calculations. International Journal of Heat and Mass Transfer 1989;32:1605–18.

[105] Stanmore BR, Brilhac JF, Gilot P. The oxidation of soot: A review of experiments, mechanisms and models. Carbon 2001;39:2247–68.

[106] Trubetskaya A, Timko MT, Umeki K. Prediction of fast pyrolysis products yields using lignocellulosic compounds and ash contents. Applied Energy 2020;257:113897.

[107] Tsai WT, Lee MK, Chang YM. Fast pyrolysis of rice straw, sugarcane bagasse and coconut shell in an induction-heating reactor. Journal of Analytical and Applied Pyrolysis 2006;76:230–7.